Contributions to Mineralogy and Petrology (2022) 177:44
https://doi.org/10.1007/s00410-022-01905-w

ORIGINAL PAPER

COH-fluid induced metasomatism of peridotites in the forearc mantle

Melanie J. Sieber[1,2] · Gregory M. Yaxley[1] · Jörg Hermann[3]

Received: 24 January 2022 / Accepted: 28 February 2022

Abstract
Devolatilization of subducting lithologies liberates COH-fluids. These may become partially sequestered in peridotites in the slab and the overlying forearc mantle, affecting the cycling of volatiles and fluid mobile elements in subduction zones. Here we assess the magnitudes, timescales and mechanism of channelized injection of COH-fluids doped with Ca^{2+}_{aq}, Sr^{2+}_{aq} and Ba^{2+}_{aq} into the dry forearc mantle by performing piston cylinder experiments between 1–2.5 GPa and 600–700 °C. Cylindrical cores of natural spinel-bearing harzburgites were used as starting materials. Based on mineral assemblage and composition three reaction zones are distinguishable from the rim towards the core of primary olivine and orthopyroxene grains. Zone 1 contains carbonates + quartz ± kyanite and zone 2 contains carbonates + talc ± chlorite. Olivine is further replaced in zone 3 by either antigorite + magnesite or magnesite + talc within or above antigorite stability, respectively. Orthopyroxene is replaced in zone 3 by talc + chlorite. Mineral assemblages and the compositions of secondary minerals depend on fluid composition and the replaced primary silicate. The extent of alteration depends on fluid CO_2 content and fluid/rock-ratio, and is further promoted by fluid permeable reaction zones and reaction driven cracking. Our results show that COH-fluid induced metasomatism of the forearc mantle is self-perpetuating and efficient at sequestering Ca^{2+}_{aq}, Sr^{2+}_{aq}, Ba^{2+}_{aq} and CO_{2aq} into newly formed carbonates. This process is fast with 90% of the available C sequestered and nearly 50% of the initial minerals altered at 650 °C, 2 GPa within 55 h. The dissolution of primary silicates under high COH-fluid/rock-ratios, as in channelized fluid flow, enriches SiO_{2aq} in the fluid, while CO_{2aq} is sequestered into carbonates. In an open system, the remaining CO_2-depleted, Si-enriched aqueous fluid may cause Si-metasomatism in the forearc further away from the injection of the COH-fluid into peridotite.

Keywords Carbonation · Deep carbon cycle · COH-fluid · Forearc · HP-experiments

Introduction

Volumetrically significant metasomatism takes place in subduction zones because of the juxtaposition and interaction among disparate lithologies. Metasomatism is, for instance, driven by activity gradients when fluids, released from the subducting slab, move along variable pressure/temperature-trajectories and are injected into lithologies other than their source region (Bebout and Barton 1989; Bebout 2013; Stern 2002). Such fluid injection and related mass transfer and metasomatism are particularly relevant at the slab–mantle interface (e.g., mélange zones; Breeding et al. (2004)) and when fluids are injected into the hanging wall of the overlying, ultramafic mantle. Subducting (meta-) sediments and altered oceanic crust are a source of CO_{2aq} and volatile elements for metasomatising fluids particularly when they are infiltrated by externally derived aqueous fluids (Gorman et al. 2006).

The flux and CO_2-concentrations of COH-fluids released from the subducting slab are poorly known, which is partially related to different approaches used for constraining CO_2 concentrations in fluids liberated from the subducting slab. For instance, Kelemen and Manning (2015) re-evaluated and compiled C-fluxes and calculated fluid compositions expelled from the subducting plate by estimating the

Communicated by Othmar Müntener.

✉ Melanie J. Sieber
sieber.m.j@gmail.com

[1] Research School of Earth Science, The Australian National University, Canberra 2601, Australia

[2] Present Address: Institute of Geosciences-Mineralogy, University Potsdam, 14476 Potsdam-Golm, Germany

[3] Institute of Geological Science, University of Bern, 3012 Bern, Switzerland

Published online: 05 April 2022

amount of aqueous fluids released and modelling the solubility of carbon in aqueous fluids. According to these authors, the C-fluxes depend on the amount of released water and the solubility of calcite and aragonite into aqueous fluid. They supposed that the molar proportion of CO_2 in a CO_2 and H_2O fluid ($X_{CO_2}^{fluid}$) is ≤ 0.001 between 0.5 and 2 GPa. As the solubility of carbonates in aqueous fluids increases with increasing pressure and temperature (Caciagli and Manning 2003; Dolejs and Manning 2010) fluids liberated between 2 and 6 GPa have higher $X_{CO_2}^{fluid}$ ranging from around 0.008 to 0.012 if dissolution of carbonation into aqueous fluids is assumed to be the single process contributing carbon to fluids (Kelemen and Manning 2015). Note that mineral decarbonation reactions may also release carbon into hydrous melts (Martin and Hermann 2018; Poli 2015) and must also be considered when estimating total C-fluxes (Kelemen and Manning 2015). Phase equilibria studies report a ~ 700 times higher CO_2 concentration in fluids liberated under the forearc. Despite the increase in solubility, the experimental approach of Molina and Poli (2000) and Poli et al. (2009) showed that progressive decomposition of hydrated phases with continuing subduction is coupled with increasing stability of carbonates. Thus, fluids released under the forearc contain more CO_2 ($0.04 < X_{CO_2}^{fluid} < 0.4$; ~ 1–2 GPa and ~ 650–750 °C) compared to fluids released at higher presssures ($X_{CO_2}^{fluid} < 0.2$; 2.2–5 GPa and 680–800 °C) (Molina and Poli 2000; Poli et al. 2009). Thermodynamic models of phase equilibria in closed and open systems support those experimental results (Connolly 2005; Gorman et al. 2006; Kerrick and Connolly 2001a, b).

Peridotites are suitable for sequestering some of the released CO_{2aq} as carbonate minerals, because of their abundance of divalent metal ions, required for carbonate mineral formation (Kelemen et al. 2011). Seawater alteration of peridotites typically forms Ca-rich carbonates (calcite and aragonite) (Grozeva et al. (2017), while alteration of peridotites by metamorphic fluids released during subduction forms Mg-rich carbonates (dolomite and magnesite) (Menzel et al. 2018; Sieber et al. 2018). The latter is accompanied by the formation of talc, quartz, and fuchsite (Cr-muscovite) along with Fe-oxide, -hydroxide, and/or sulfide phases (Falk and Kelemen 2015; Menzel et al. 2018).

Ophiolites record the importance of such COH-fluid/peridotite interaction in the forearc. For instance, fully carbonated peridotites have been reported from ophiolite complexes as soapstones (carbonate + talc rocks) and listvenites (carbonate + quartz rocks) formed under pressures and temperatures of 0.2–1.5 GPa and 80–350 °C (e.g., Samail ophiolite: Falk and Kelemen (2015); Linajavri and Leika ophiolite: Beinlich et al. (2012); Bjerga et al. (2015); Advocate ophiolite complex: Menzel et al. (2018)). Carbonation of subducted rocks also occurs under blueschist and eclogite facies conditions as reported, for instance, from marbles from Corsica (France), which are interpreted to be formed by percolation of carbonic fluids through Ca–Mg silicate rocks during subduction at temperatures of 450–500 °C and pressures of ~ 1.5 GPa (Piccoli et al. (2018); Piccoli et al. (2016)). Ague and Nicolescu (2014) reported carbonation of blueschists and metapelites at ~ 500–550 °C and ~ 2 GPa from the Cycladic subduction complex exposed on Syros and Tinos island (Greece). Even higher temperatures and pressures of ~ 550–600 °C and ~ 2.3–2.5 GPa are reported for "high pressure ophicarbonates" from the Ligurian Voltri Massif (Italy) (Scambelluri et al. 2016). In addition, the reduction of carbonates by hydrogen-bearing fluids to elemental carbon and methane is reported from high pressure ophiocarbonates (Brovarone et al. 2017; Galvez et al. 2013a, b; Malvoisin et al. 2011). Thus, the redox budget is essential for the mobility of carbon in fluids.

Those field observations have in common a close local relationship between the liberation of carbon into COH-fluids during subduction and carbon sequestration by COH-fluid driven carbonation of ultramafic rocks. However, the extents, reaction mechanism and fluid pathways are poorly constrained. In particular, since the reaction mechanism for the formation of fully carbonated peridotites (soapstones and listvenites) at shallow depths is unclear, it is not known how carbonation operates under higher pressures corresponding to depths of ~ 30–75 km. One of the most important, but not yet fully understood contradictions regards the high efficiency of peridotite carbonation in the light of decreasing permeability with ongoing carbonation. Alteration of peridotites increases the solid volume and thus may inhibit formation of permeability. Furthermore, an armouring reaction limiting interface has been observed in mineral carbonation experiments performed at low pressures and temperatures (Kelemen et al. 2011; King et al. 2010). Nonetheless, fully carbonated peridotites (listvenites, soapstones) exist. Their formation can be explained if carbonation is non-isochemical and some material is transported away by the interacting fluid or if reaction driven cracking occurs (Putnis 2009; Putnis and John 2010; Putnis and Putnis 2007).

To better constrain reaction pathways, and the extent and mechanism of peridotite alteration, we present the first experimental investigation of peridotite carbonation between 1–2.5 GPa and 600–700 °C using cylindrical cores of natural spinel-bearing harzburgites surrounded by a free, carbon-saturated COH-fluid. The high fluid/rock-ratios of the experiments simulate channelized fluid flow. Using natural peridotites in the experiment allows simulation of fluid/rock interaction under natural grain sizes, grain shapes, anisotropy and texture of the rocks. This study shows that extensive peridotite hydration and carbonation in the forearc is feasible as fluid permeable reaction zones are formed. The extent of alteration,

reaction mechanisms and evolution of reaction zones and fluid composition over time are discussed.

Analytical methods and modelling

Phase proportions and mineral compositions of the untreated peridotite sample (PO6) used in the experiments were analysed by powder X-ray Diffraction (XRD), Scanning Electron Microscopy (SEM), Electron-Probe Micro Analysis (EPMA) and Laser Ablation Inductively Coupled Plasma Mass Spectrometry (LA-ICP-MS). The composition of the quenched fluid of run 42 was analysed by gas chromatography for CO_2, H_2O and alkanes (from methane to hexane). The method is described in detail in Sieber et al. (2018). High-resolution, X-ray Computed Tomography (CT) was performed for the same experiment (run 42). Raman spectroscopy verified the presence of graphite with low crystallinity, which will be referred to as elemental carbon. EPMA, SEM and LA-ICP-MS were used to quantify the compositions of minerals and reaction zones. Furthermore, elemental maps were obtained using Wavelength and Energy Dispersive Spectrometry (EDS, WDS) for selected regions of interest and computed with the software XMapTools (Lanari et al. 2014). Details of the analytical methods are reported in the supplementary information. Reported Mg# are defined by 100×Mg/(Mg+totalFe) without correction for Fe^{3+}.

Thermodynamic modelling was performed with the software package perple_X (version 6.7.5) using the hp02ver.dat database and the C-saturated COH MRK hybrid equation of state for the fluid (Connolly and Cesare 1993; Connolly 2005; Holland and Powell 1998). Solid solution models for brucite, clinopyroxene, chlorite, dolomite, magnesite, olivine, orthopyroxene, spinel and talc after Holland and Powell (1998) and antigorite after Padrón-Navarta et al. (2013) were applied. Phase equilibria were computed in the MgO–FeO–Al_2O_3–SiO_2–CaO system under COH-fluid saturation. Phase diagrams were computed as a function of quartz activity and molar O/(O+H) ratio in the fluid (X_O^{fluid}) using the MgO–FeO–Al_2O_3 composition of primary olivine and orthopyroxene. X_O^{fluid} is imposed by the relative amounts of volatiles in the experimental fluid. The formation of methane and elemental carbon is observed in the experiments and reduces CO_{2aq} but maintains X_O^{fluid} (Connolly and Cesare 1993; Huizenga 2011). The modelling considers crystalline graphite, but poorly ordered graphite was observed in the experiment which may lead to a slightly different COH fluid speciation (Tumiati et al. 2020).

Experimental strategy and starting material

Starting material

The peridotite xenoliths (sample PO6) used as starting material in the high pressure (P) and temperature (T) experiments is from the Potrillo volcanic field in New Mexico and was selected, because it is unaltered (only very minor amphibole exists) and has an equigraniular texture with grain sizes around 1 mm. Modal abundances of olivine (81 wt%), orthopyroxene (15 wt%) and clinopyroxene (4 wt%) with minor spinel, obtained from powder XRD classifies sample PO6 as spinel-bearing harzburgite. The chemical composition of primary phases is typical for a mantle derived harzburgite (Table 1). Cylindrical cores of the spinel-bearing harzburgite were drilled and sanded. The peridotite cores were neither fractured, nor washed, nor 'cleaned' of alteration products before the experiment as is common in studies investigating in-situ CO_2 sequestration related to carbon capture and storage to enhance the reaction surface (Lacinska et al. 2017). However, minor fractures introduced by the sample preparation are likely.

Experimental setup

Cylindrical cores (radius ~ 2 mm; length ~ 4–7 mm) of natural peridotite (sample PO6) were used to simulate the COH-fluid driven carbonation of peridotites in the forearc mantle wedge. Experiments were performed at 1.0, 2.0 and 2.5 GPa and 600–700 °C for 48–192 h (Table 2) using a conventional MgO–graphite–NaCl assembly in 12.7 mm end-loaded piston cylinder presses at the Research School of Earth Science (the Australian National University). The pressure and temperature allow comparison between experiments run within (≤ 2.5 GPa, ≤ 650 °C) and above (2.5 GPa, 700 °C) antigorite stability (according to thermodynamic calculation).

The peridotite-cores underlain by a mixture of oxalic acid dihydrate ($C_2H_2O_4 \cdot 2H_2O$) and Ba-, Sr-, Ca-carbonates and PbO were set into thick-walled Ag-capsules with an inner volume of ~ 95 mm^3 (same experimental setup as Sieber et al. (2020)). The capsules were topped up with deionized water. This experimental setup with relatively high fluid/rock-ratios (0.39–1.08) was used to simulate channelized fluid flow in the slab and mantle wedge between a free fluid (presumably occurring in the fluid channel) and a peridotite. This setup is testing the effectiveness of carbonation in a less favourable arrangement for sequestration of volatiles compared to porous flow with a much larger reactive surface. Fluid mobile elements (Ba, Sr, Ca and Pb) were added, because they are released from

Table 1 Major and trace element composition of enstatite, diopside, olivine, olivine and spinel are listed before and after treatment

Primary phases before the experiment									Primary phases after the experiment								
	Enstatite		Diopside		Olivine		Spinel			Enstatite		Diopside		Olivine		Spinel	
	Average	2σ	Average	2σ	Average	2σ	Average	2σ		Average	2σ	Average	2σ	Average	2σ	Average	2σ
SiO_2 [wt%]	56	1	53	1	41	1	< 0.04		SiO_2 [wt%]	56	1	54	1	40.8	0.4	0.1	0.1
TiO_2 [wt%]	0.08	0.07	0.3	< 0.03	< 0.03		0.1	< 0.02	TiO_2 [wt%]	< 0.03		< 0.03		< 0.03		< 0.03	
Al_2O_3 [wt%]	4.3	0.3	5.6	0.2	< 0.03		49.7	0.5	Al_2O_3 [wt%]	4	1	5	2	0.5	0.8	49.9	1.0
Cr_2O_3 [wt%]	0.6	0.1	1.1	0.1	< 0.03		17.9	< 0.04	Cr_2O_3 [wt%]	0.7	0.3	0.9	0.3	< 0.03		18	1
FeO [wt%]	5.8	0.1	2.7	0.1	9.0	0.2	10.9	< 0.05	FeO [wt%]	5.7	1.0	4.4	1.3	8.8	0.9	10.8	0.6
MnO [wt%]	0.1	< 0.02	0.1	< 0.02	0.1	< 0.02	< 0.04		MnO [wt%]	0.0	0.1	< 0.03		0.0	0.1	< 0.04	
MgO [wt%]	33.3	0.4	16.2	0.4	50.1	0.6	19.7	0.3	MgO [wt%]	33	4	27	8	50	2	20	1
CaO [wt%]	0.9	< 0.05	20.0	0.3	0.1	0.1	< 0.03		CaO [wt%]	1.8	4.2	7.4	9.4	0.7	0.7	< 0.03	
NiO [wt%]	0.1	< 0.03	< 0.04		0.40	0.03	0.3	< 0.01	NiO [wt%]	0.1	0.1	< 0.04		0.34	0.05	0.1	0.2
Na_2O [wt%]	0.1	< 0.03	1.2	< 0.05	< 0.02		< 0.02		Na_2O [wt%]	0.2	0.1	1.2	0.1	0.11	0.02	< 0.02	
K_2O [wt%]	< 0.02		< 0.02		< 0.02		< 0.02		K_2O [wt%]	< 0.02		< 0.02		< 0.02		< 0.02	
P_2O_5 [wt%]	< 0.03		0.4	0.1	< 0.03		< 0.03		P_2O_5 [wt%]	< 0.03		< 0.03		< 0.03		< 0.03	
Total [wt%]	102	2	101	2	101	1	98.7	0.7	Total [wt%]	100	1	101	1	100	2	98.8	2.1
Sc [ppm]	19.7	0.5	64	1	3.8	0.2	nA		Sc [ppm]	22	1	62	62	6	3	nA	
Cr [ppm]	3868	335	7830	290	108	6	nA		Cr [ppm]	3787	245	8002	8004	105	6	nA	
Mn [ppm]	983	22	641	25	963	29	nA		Mn [ppm]	1016	9	649	661	984	59	nA	
Co [ppm]	60	1	23.2	0.4	144	5	nA		Co [ppm]	60	1	23	23.0	143	7	nA	
Ni [ppm]	802	34	390	8	3101	107	nA		Ni [ppm]	535	129	387	390	1979	1191	nA	
Sr [ppm]	0.1	< 0.01	21	0.5	< 0.01		nA		Sr [ppm]	0.1	0.0	38	57.5	< 0.01		nA	
Ba [ppm]	< 0.01		0.1	0.3	< 0.01		nA		Ba [ppm]	< 0.01		26.3	58.0	< 0.01		nA	
Pb [ppm]	< 0.01		< 0.01		< 0.01		nA		Pb [ppm]	< 0.01		1.5	3.9	< 0.01		nA	

nA not analyzed

Table 2 Listed are the experimental run conditions, the fluid composition considering the formation of elemental carbon as described in the text and the phase assemblage of the reaction zones (1, 2 and 3) for all experiments

	Run 35	Run 34	Run 39	Run 42	Run 36	Run 37
Run conditions						
Pressure [GPa]	1	2	2	2.5	2.5	2.5
Temperature [°C]	600	600	600	650	700	700
Run duration [h]	48	192	192	55	72	192
Fluid composition considering the formation of elemental carbon						
H_2O [mol%]	81	83	74	83	74	76
CO_2 [mol%]	19	17	26	17	26	24
Xo	0.42	0.41	0.46	0.41	0.46	0.45
Fluid/rock						
Mass ratio	0.39	0.41	0.77	0.54	0.35	1.08
Zone 1		carb, ± qtz, ± ky				
Zone 2						
Olivine	tlc, mag	serp, mag	tlc, mag	tlc, mag	tlc, mag	tlc, mag
Orthopyroxene	tlc, mag, ± chl	tlc, mag, ± chl	tlc, mag, chl	tlc, mag, chl	tlc, mag, chl	tlc, mag, chl
Clinopyroxene	tlc, mag, ± chl	tlc, mag, ± chl	no cpx relict	tlc, mag	tlc, mag, Mg-cal, chl	no cpx relict
Zone 3						
Olivine	n.o	n.o	serp, ± mag	serp, mag, tlc	n.o	n.o
Orthopyroxene	n.o	n.o	tlc, chl, ± carb	n.o	n.o	tlc, chl

carb carbonates, *chl* chlorite, *cpx* clinopyroxene, *ky* kyanite, *mag* magnesite, *Mg-cal* Mg-calcite, *n.o.* not observed, *serp* serpentine, *tlc* talc, *qtz* quartz

sediments and altered oceanic crust into a fluid during subduction. Furthermore, the partition coefficients between COH-fluid and magnesite are known for these elements (Sieber et al. 2018) and thus the trace element content in newly formed magnesite can be used to monitor the evolution of the fluid.

Fluid composition

Oxalic acid dihydrate dissociates during heating to CO_2, H_2O and H_2 in a molar ratio of 2:2:1 (Morgan et al. 1992). Earlier time series experiments on the COH-fluid driven carbonation of serpentinites performed under the same *PT*-conditions and using the same experimental setup showed, that such a CO_2–H_2O–H_2 fluid forms elemental carbon and some methane at the start of the experiment before antigorite carbonation initiates (Sieber et al. 2020). Here, the formation of elemental carbon and methane is also observed (see "Results"), indicating that also in this set of experiments H_2 was consumed by the reduction of CO_{2aq} at the onset of the experiments. The use of thick-walled Ag-capsules together with the relatively low run temperatures (max 700 °C) minimizes the loss of initially produced H_2 and also minimizes H_2 loss during the ongoing experiment (Hack and Mavrogenes 2006; Spandler et al. 2007). The initial fluid composition was calculated (Table 2), assuming that all available hydrogen reduces CO_{2aq} to elemental carbon before the fluid starts to react with the solids and neglecting the formation of small amounts of methane. The presence of an aqueous fluid together with minor CO_{2aq} and CH_4 coexisting with elemental carbon is characteristic for the "water maximum" in the COH system and constrains oxygen fugacity to about 1 to 2 log units below the QFM buffer (Foley 2011). Using the oxybarometer of Miozzi and Tumiati (2020) the oxygen fugacity for the CO_2–H_2O fluids saturated with glassy carbon at 2 and 2.5 GPa is about 0.1 to 0.2 log units below QFM buffer. Assuming complete dissolution of Ba-, Sr-, Ca-carbonates and PbO into the fluid, the CO_2–H_2O fluid is expected to contain 2.5 mol% Ca^{2+}_{aq}, 0.2 mol% Sr^{2+}_{aq}, 0.1 mol% Ba^{2+}_{aq} and 0.1 mol% Pb^{2+}_{aq} except for run 42, where the expected concentrations of Sr^{2+}_{aq} Ba^{2+}_{aq} and Pb^{2+}_{aq} are 2 to 14 times smaller. The concentrations of Sr, Ba and Pb in the primary silicates (Table 1) are negligible in comparison to the concentrations in the fluid.

Results

Reaction products and replacement textures

Hydration and carbonation of primary silicates are evident in the formation of secondary phases but relicts of primary

phases remain. Relicts of primary clinopyroxene are rare, which might be caused by their minor abundance (4 wt%, per XRD) in the harzburgite or may indicate complete replacement.

The extent of alteration (= abundance of secondary solids relative to primary solids) depends on the initial fluid/rock-ratio, the composition of the fluid, pressure and temperature. Furthermore, the extent of replacement may increase over the run duration, as implied by comparing BSE-images of run 34 and 35 (Fig. 1a, b). Run duration (192 h vs 48 h) marks the main difference between those experiments performed with similar fluid/rock-ratio and fluid composition (Table 2). Higher temperature seems to also enhance the extent of replacement. For instance, in run 39 (2 GPa, 600 °C; Fig. 2) olivine grains are still preserved and the grain size of remaining orthopyroxene is larger compared to orthopyroxene grains in run 37, where no relicts of olivine grains are found (2.5 GPa, 700 °C; Fig. 3). Higher fluid/rock-ratios may also enhance the extent of alteration and the amount of carbonates depends on the CO_2 budget of the initial fluid. For instance, the replacement of olivine is more pronounced in run 39 compared to run 34, performed under same *PTt* conditions, but higher initial fluid/rock ratios (Fig. 1a, e, f). We note that many observations are only qualitative and have to be considered with care as they are based on 2D cross sections of the recovered cores and not on 3D images. However, overall the extent of replacement is remarkable and reaction zones are often several hundreds of µm in width (Fig. 1). Phase segmentation of the CT-scan of run 42 that ran for only 55 h reveals an abundance of 46 vol% for secondary solids.

Replacement of primary silicates occurred at the reaction interface, where the fluid was in contact with primary silicates and is recorded in the formation of newly formed phases. Etch pits are formed at the contact between remnant and secondary silicates (Fig. 1c) and may indicate faster dissolution along certain crystallographic directions (Hövelmann et al. 2011; King et al. 2010; Velbel and Ranck 2008). The reaction interface proceeds with time (progressing reaction) from the primary grains' surface towards the core. Thus, primary phases are most strongly (up to completely) replaced at the margins of the cores and partially replaced towards the centre of the cores (Figs. 1, 2, 3). Replacement is pronounced at the rims of primary silicates (Figs. 1, 2, 3, 4, 5) and along fluid channels cross cutting primary grains.

Three reaction zones are distinguishable by means of their secondary mineral assemblages, mineral modes, bulk and mineral composition, and texture. Secondary phases are carbonates (magnesite, Mg–calcite), quartz, talc, antigorite, chlorite, kyanite and elemental carbon. Except for run 36 and 42, in which quartz and kyanite have not been observed, those phases are present in all runs. The reaction zones are here described from the secondary replacement rim to the relict core of primary silicates and listed in Table 2.

Zone 1: carbonates + quartz ± kyanite

At their pristine surface, primary grains react to carbonates + quartz ± kyanite (Fig. 4a, b). Kyanite is associated with the replacement of pyroxenes, but absent in the replacement of olivine grains. Zone 1 contains elemental carbon (Fig. 5d), which is also present at the outside of all cores and inside walls of the capsules. Anhedral grains of carbonates, quartz and kyanite, if present, have an intermingled texture. Quartz is rare and fine grained in run 34 and absent in run 36 and 42. Zone 1 is pronounced in experiments with a high initial fluid/rock-ratio (> 0.54) and here massive quartz-layers (height ~ 0.5–1 mm) are formed. Quartz-layers occur at the bottom of the capsules (Figs. 2, 3), where temperatures might be 5–10 °C lower (Hack and Mavrogenes 2006; Spandler et al. 2007) so that quartz could precipitate. The quartz-layers contain fragments of primary spinel and newly formed kyanite (1–30 µm), magnesite and dolomite (10–40 µm; Fig. 3c, d). Within the quartz-layers, spinel reacts to kyanite (Fig. 3d) indicating the formation of quartz before quenching. The precipitation of quartz away from the peridotite-core (at the bottom of the capsule) demonstrates mass transport by the fluid. In experiments with quartz-layers (run 37, 39), radial grains of dolomite (< 30 µm) and some quartz (< 20 µm) crystals are randomly distributed within the capsules. Those may have been transported as precipitates within the fluid during the experiment or may have formed upon quenching (Fig. 3e).

Zone 2: carbonates + talc ± chlorite

Adjacent to zone 1, carbonates + talc ± chlorite mimic the shape of primary silicates (Figs. 1c, d, 4a, b). In zone 2, carbonates and talc are spatially separated from each other, with magnesite occurring more towards the former grain surface (and towards zone 1, if present) and talc occurring towards the centre of the grain (towards the primary phase, if it remains) (Fig. 4a, b). Chlorite is present in the replacement of pyroxenes, but nearly absent in the replacement of olivine. Chlorite, if present, is intermingled with talc and magnesite (Fig. 4b). Some elemental carbon might be present in zone 2 (Fig. 5d). In run 34, olivine grains are replaced by antigorite + magnesite rather than talc + magnesite.

Zone 3: hydrous phases dominate

Zone 3 is only present in experiments with a high initial fluid/rock-ratio (≥ 0.54; Table 2) and the mineral assemblage depends on the *PT*-conditions. At 600 °C and 2 GPa, antigorite with minor magnesite replaces olivine (run 39; Fig. 4a).

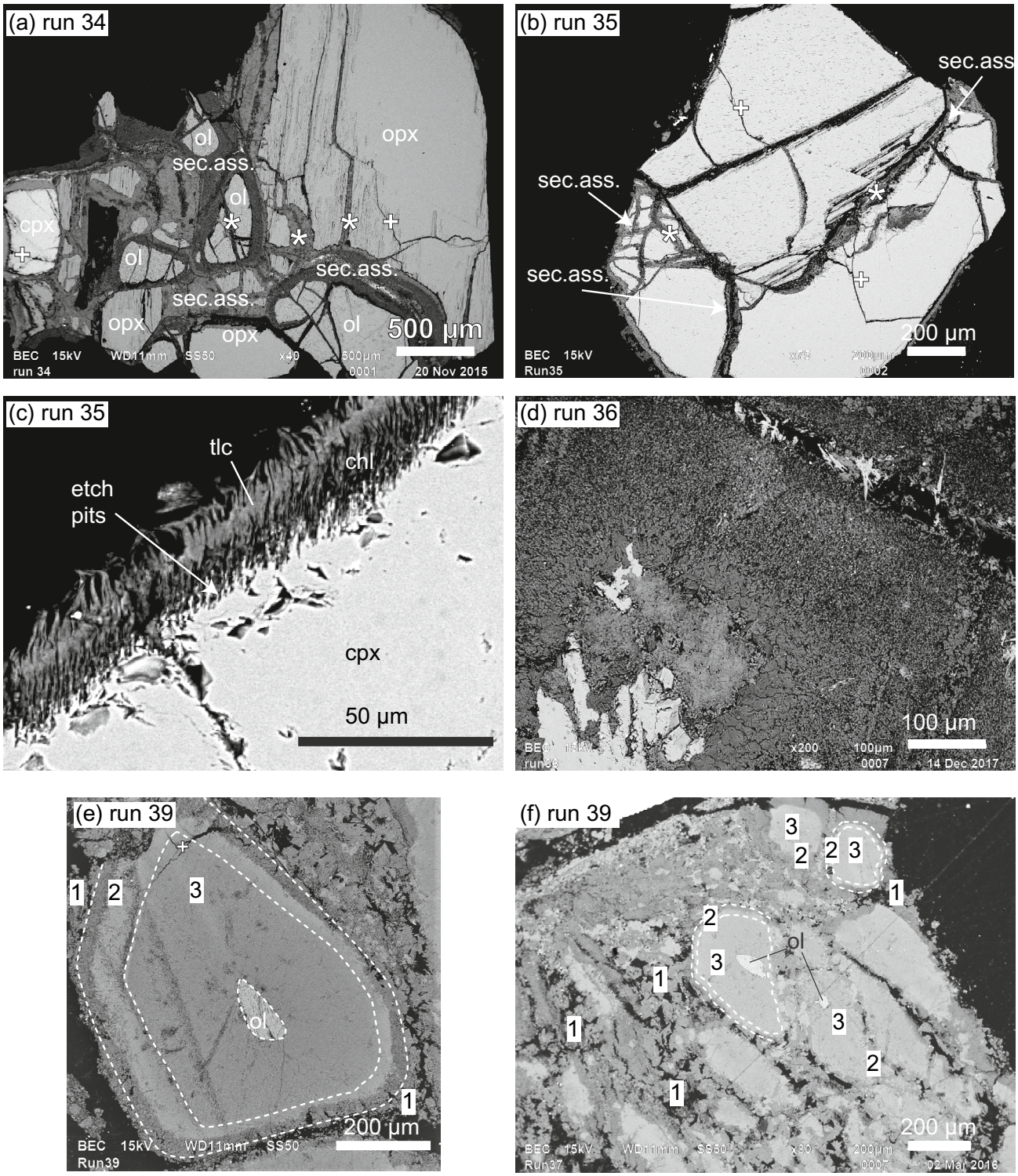

Fig. 1 BSE-images of run products. Secondary assemblages (sec.ass.) replace primary silicates (*ol* olivine, *cpx* clinopyroxene, *opx* orthopyroxene). **a**, **b** Increasing abundance of secondary phases over time **a** 192 h, **b** 48 h; reaction driven cracking marked with * implied by the presence of zone 2 but absence of zone 1, decompression fractures (+) are not filled by secondary minerals; **c** etch pits are formed in the replacement of *cpx* by *tlc* (talc) and *chl* (chlorite); **d**, **e** pore space is visible in reaction zones formed in a pseudomorphic replacement; **f** almost complete replacement but the initial shape of the primary silicate can still be envisioned. Numbers refer to reaction zones as described in the text

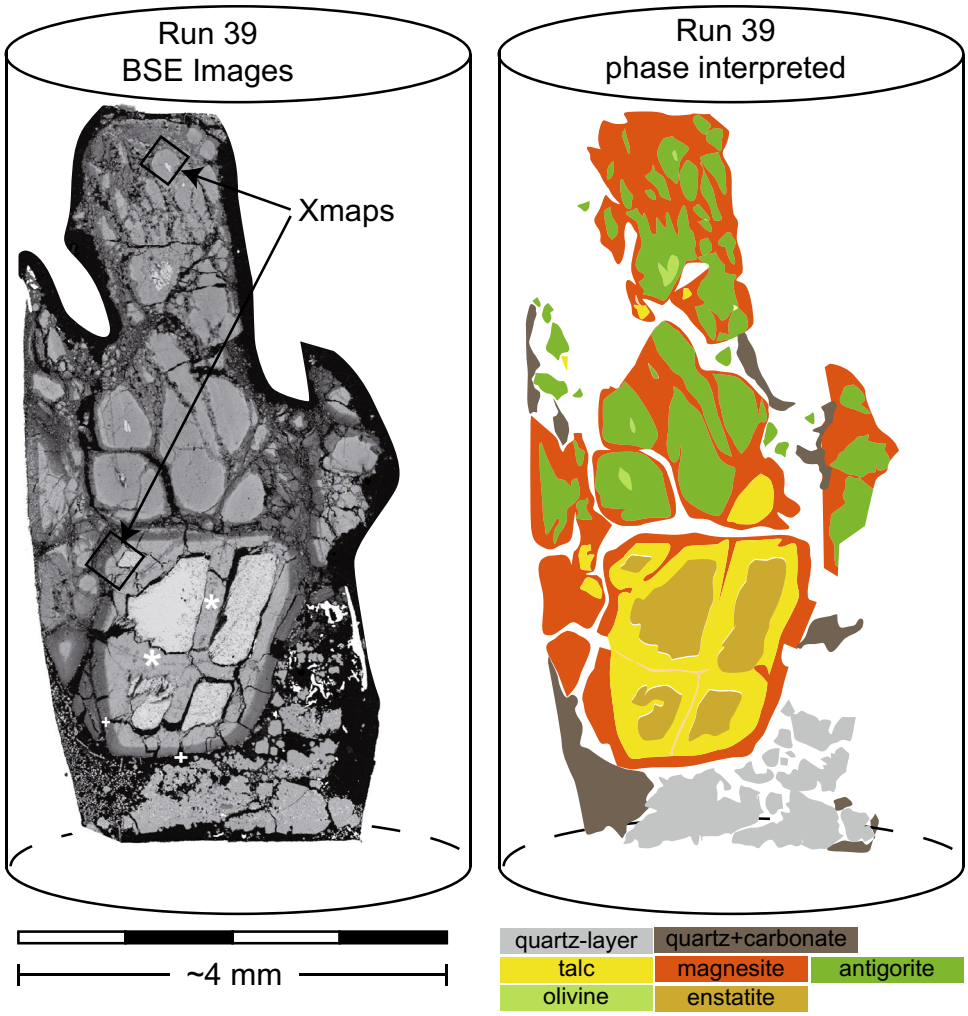

Fig. 2 Cross section through recovered peridotite core (run 39) in relation to the position within the capsule; (left) BSE-images and (right) manually colour coded phase distribution (schematically). Selected fields of interest for X-ray mapping are indicated (maps are displayed in Fig. 4). Reaction driven cracking marked as in Fig. 1

At 650 °C and 2.5 GPa, intermingled crystals of talc, antigorite and magnesite are present in the replacement of olivine (run 42; Fig. 5a). No antigorite is present above 650 °C making a clear distinction between zone 2 and 3 difficult. Pyroxene crystals are replaced by talc + chlorite (Fig. 4b) making it difficult to clearly define a boundary between zone 2 and 3. Chlorite in direct contact to the primary pyroxene might be associated with zone 3, whereas chlorite intermingled with magnesite may belong to zone 2 (Fig. 4b). The elevated Ca content at the contact with primary pyroxene grains, as visible in the element map (Fig. 6b), implies small carbonate grains coexist with chlorite.

Composition of reaction zones and minerals

The average major element composition of secondary phases is reported in Table 3 according to pressure and temperature of the experiment and associated reaction zone.

Carbonates

Zone 1: Carbonates formed together with quartz ± kyanite are the main hosts for Mg, Fe and Ca and their Mg# mimics the Mg# of primary silicates (Fig. 4c, d). Likewise, the Ca content in carbonates is indicative for the replaced primary silicates. For instance, in zone 1 and replacing orthopyroxene grains, magnesite crystals are slightly enriched in CaO (~ 1 wt%) compared to magnesite (CaO ~ 0.6 wt%) replacing olivine grains. Furthermore, olivine and orthopyroxene grains are replaced by Ca-poor magnesite, whereas carbonates replacing clinopyroxene grains are, in comparison, enriched in Ca. Entire grains of Mg–calcite are interpreted as forming from full carbonation of primary clinopyroxene grains. These fully carbonated grains are gradually zoned in Ca with highest Ca content at the rims $Ca_{\sim 0.5}Mg_{\sim 0.5}CO_3$ to $Ca_{0.1}Mg_{0.9}CO_3$ at the centre. The decreasing Ca from rim to core reflects decreasing Ca^{2+}_{aq} content as carbonation proceeds.

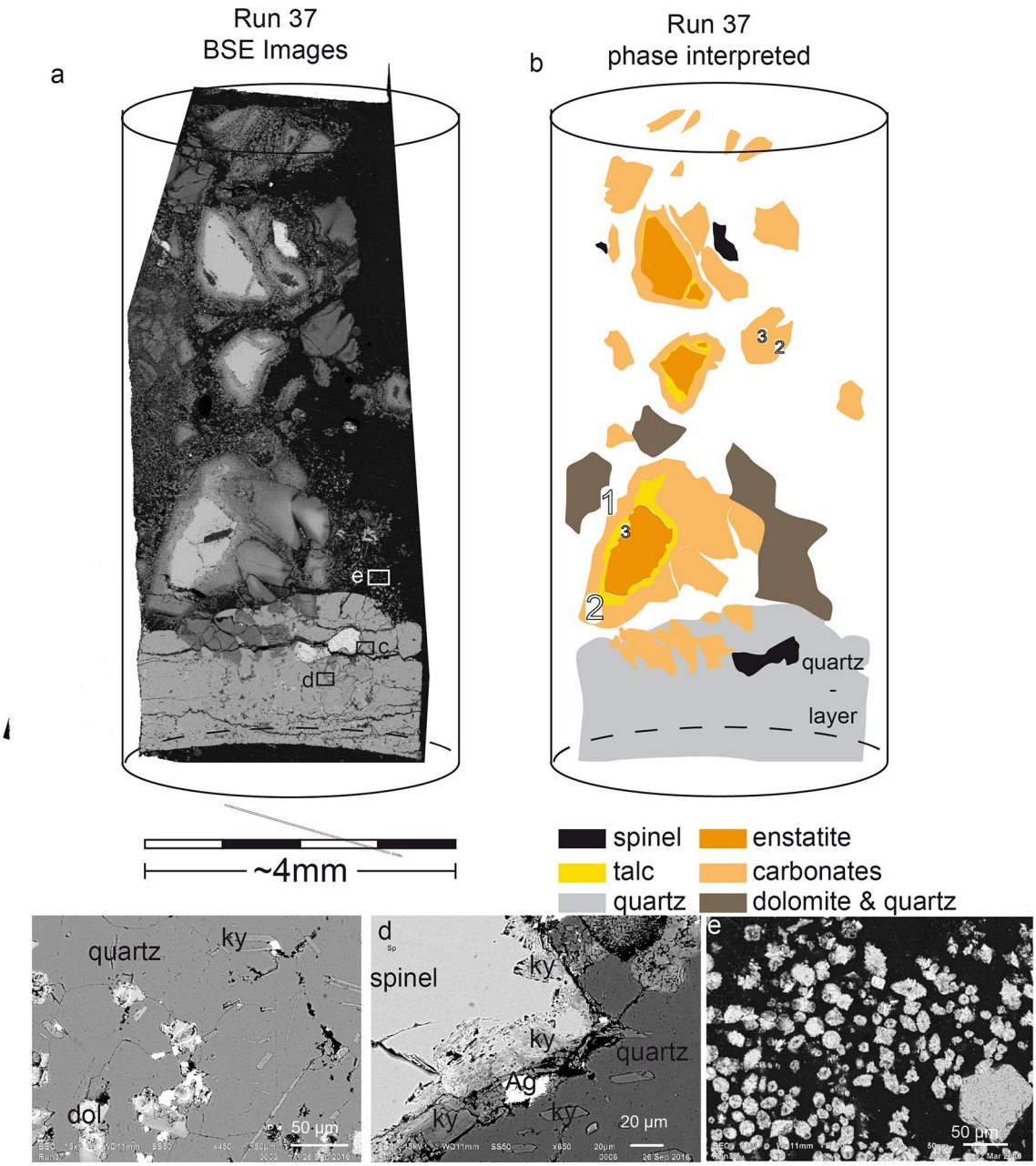

Fig. 3 **a** BSE-image of cross section through recovered peridotite core (run 37) in relation to the position within the capsule; **b** phase distribution manually colour coded schematically after BSE-images; **c** BSE-image showing dolomite (*dol*) and kyanite (*ky*) inclusions in quartz layer; **d** BSE-image of spinel reaction to kyanite (ky) within quartz layer; **e** BSE-image of dolomite and quartz crystals (either floating crystals or quench phases)

Zone 2: Magnesite grains associated with talc have lower Mg# than the replaced primary silicate, because Mg preferentially partitions into talc (Mg# = 93.5 ± 1.3 (2σ)). In zone 2, the Ca content in magnesite is lower compared to magnesite in zone 1 (Fig. 6c, d) and varies across zone 2 (Fig. 6a, b). Next to zone 1, magnesite grains contain the smallest amount of Ca (e.g., ~ 0.4 wt% Ca for the profile displayed in Fig. 6d), and their Ca content increase continuously (e.g., to ~ 0.8 wt%) towards the contact with talc.

Kyanite

Kyanite grains, if present, are associated with the replacement of pyroxenes, never with olivine.

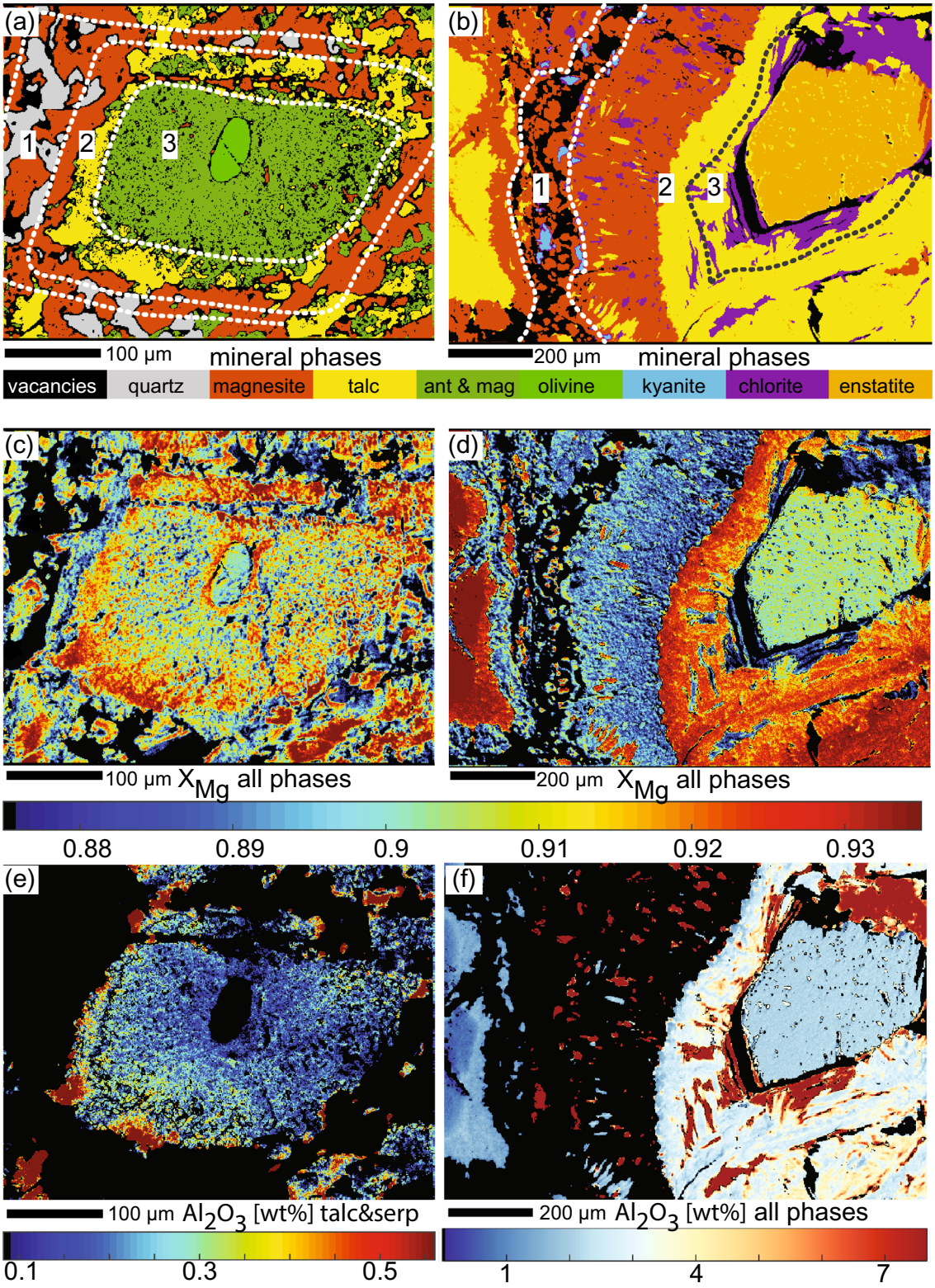

Fig. 4 Element-maps for run 39: phase interpreted X-ray map for **a** olivine and **b** orthopyroxene; **c**, **d** X_{Mg} distribution for all phases; **e** Al_2O_3 [wt%] of talc and antigorite within the olivine-map; **f** Al_2O_3 [wt%] distribution for all phases within the orthopyroxene-map

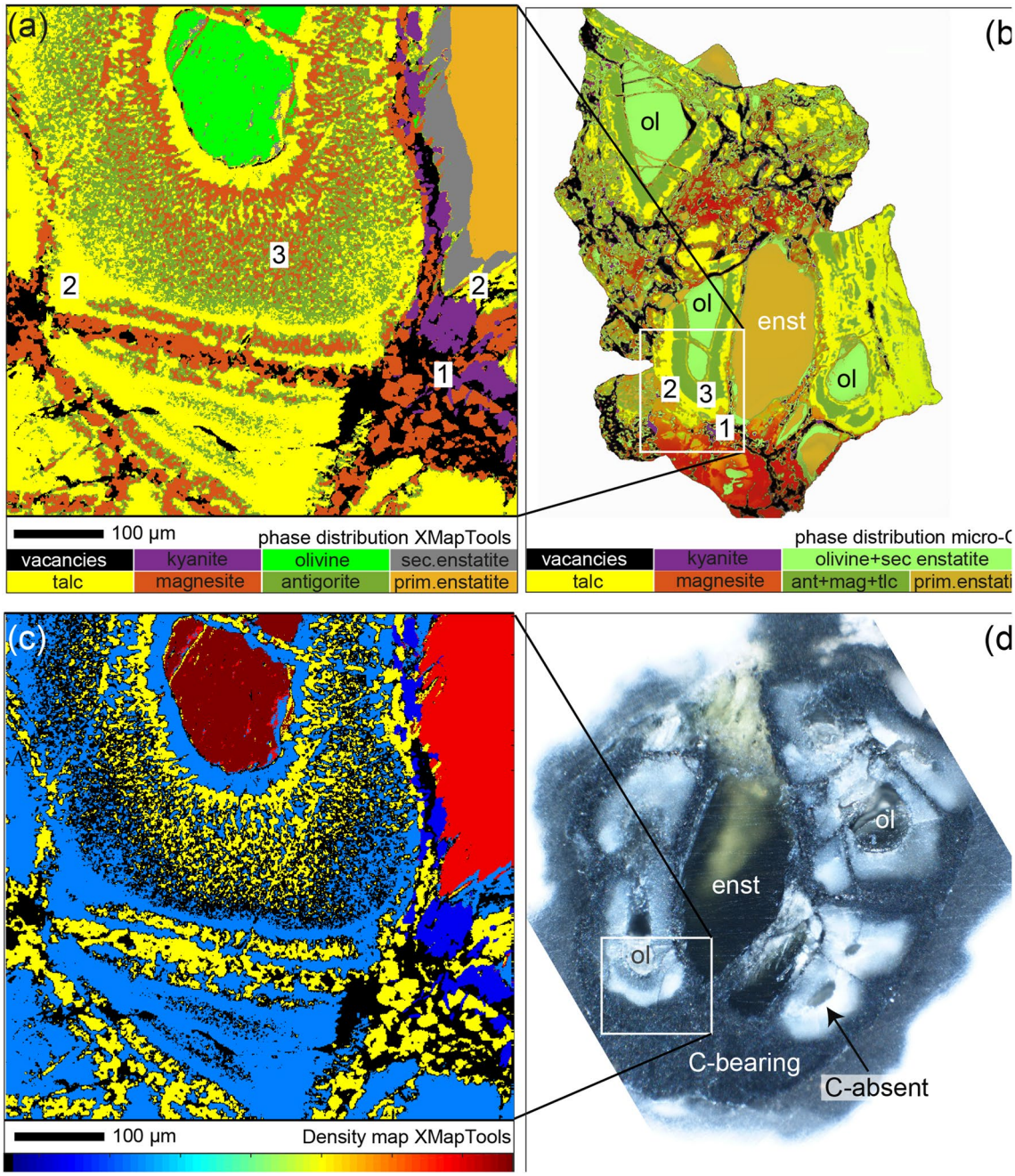

Fig. 5 **a** Phase interpreted X-ray map for run 42. Numbers refer to reaction zones, **b** phase interpreted high-resolution CT-scan; **c** density map computed by XMapTool from X-ray map displayed in **a**; **d** reflected light image of cross section showing distribution of elemental carbon (black areas)

Talc

The Mg# of talc is higher compared to the Mg# of primary silicates and gradually decreases from ~ 93 at the contact with magnesite to ~ 91 towards the primary silicate (Fig. 4c, d). Al in talc depends on the *PT*-conditions and talc replacing pyroxene has higher Al concentrations than talc replacing olivine in the same experiment. For instance, talc grains associated with the replacement of orthopyroxene (zone 2 and 3) show the highest Al concentrations of 0.32 ± 0.05 a.p.f.u. Al (for 11 oxygen) at 600 °C. Al content in talc replacing orthopyroxene decreases with increasing *PT*. At 650 °C and 2.5 GPa, talc contains on average 0.24 ± 0.03 a.p.f.u. Al and at 700 °C and 2.5 GPa the average Al content of talc is 0.18 ± 0.01 a.p.f.u.. For talc associated with the replacement of olivine grains the opposite trend is

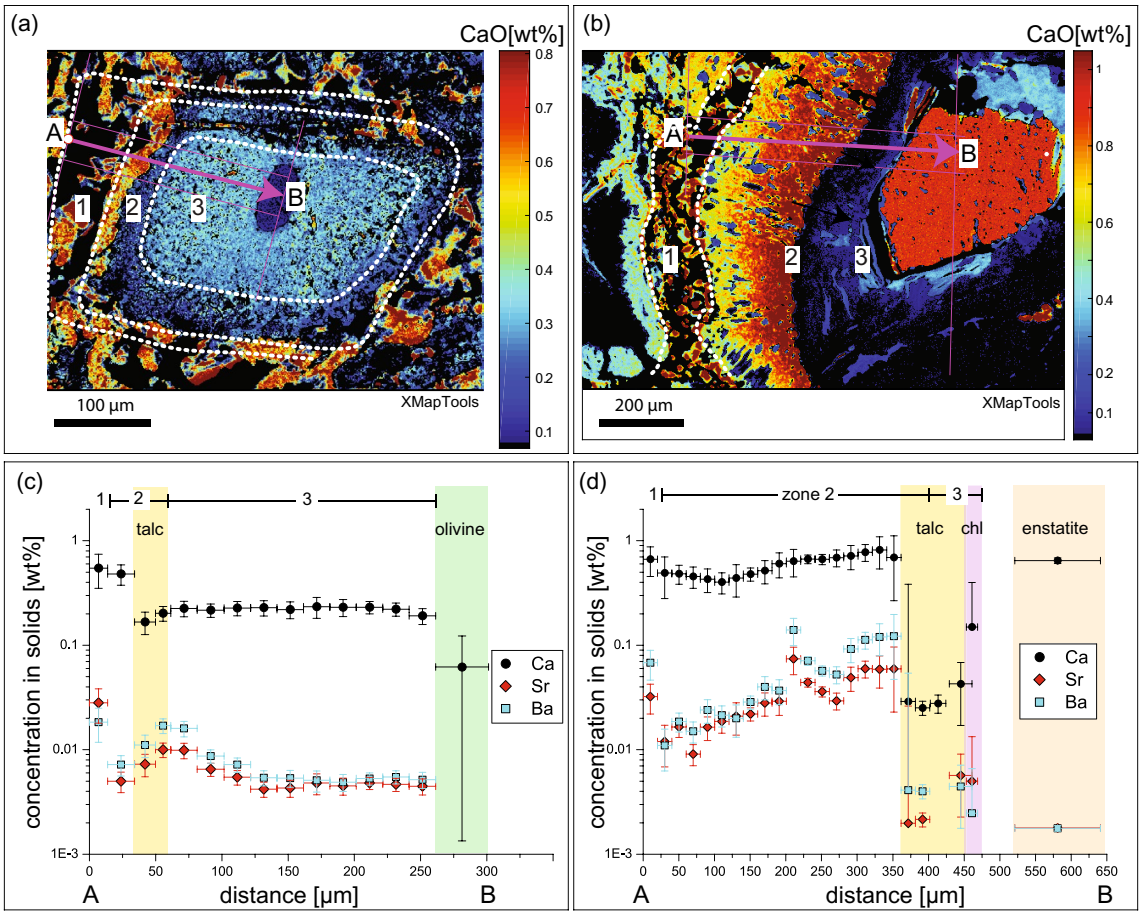

Fig. 6 CaO and trace element concentration within reaction zone for olivine (left column) and orthopyroxene (right column) in run 39. **a**, **b** CaO concentration per element mapping. Trace element compositions were measured along indicated traverses; **c**, **d** shows the segmented bulk composition. Errors in the concentrations (*y*-axis) are the 2σ deviation within 20 µm broad intervals for (**c**) and 300 µm for (**d**)

found. Here the Al content in talc increases with increasing *PT*. At 1 and 2 GPa and at 600 °C (run 34, 35, 39), the Al concentrations in talc replacing olivine are below the EPMA detection limit (~200 ppm). At higher pressure (2.5 GPa) and temperature (650 °C; run 42), talc grains replacing olivine contain on average 0.02 ± 0.01 a.p.f.u. Al. At even higher temperatures of 700 °C (run 36, 37), the average Al content in talc increases to 0.03 ± 0.01 a.p.f.u.. For the replacement of clinopyroxene no trend in the composition of talc can be reported.

Chlorite

In zone 2, chlorite crystals with Mg# ~ 93 are solely present around pyroxenes and absent in the replacement of olivine grains. Fine grained carbonates intermingled with chlorite in zone 3 may explain the slightly enhanced Ca concentrations observed in the element distribution map (Fig. 6b).

Antigorite

Al content in antigorite is below the EPMA detection limit. Antigorite at 2 GPa and 600 °C has a Mg# 91.3 ± 0.7 slightly higher than antigorite associated with talc at 2.5 GPa and 650 °C (Mg# = 90.0 ± 0.4).

Primary silicates

Olivine, orthopyroxene and clinopyroxene have Mg# of 90.8, 91.1, 91.6, respectively. Primary orthopyroxene and clinopyroxene contain 4.3 ± 0.3 wt% and 5.6 ± 0.2 wt% Al_2O_3 and 0.9 ± 0.05 wt% and 20.0 ± 0.3 wt% CaO, respectively. The peridotite sample (PO6) is out of equilibrium under the experimentally higher pressures and lower temperatures compared to its equilibrium *PT* of ~ 0.9 GPa and 1000–1100 °C (see supplementary information for geothermobarometry). Recrystallization to secondary orthopyroxene and clinopyroxene occurred in run 36 and 42 demonstrating

Table 3 Average major element composition of secondary phases are shown according to the *PT*-condition of the experiments and the associated reaction zone

	Magnesite zone 1		Magnesite zone 1		Magnesite zone 1		Kyanite* zone 1		Magnesite zone 2+3		Magnesite zone 2+3		Magnesite zone 2+3		Magnesite zone 2+3	
	2 GPa, 600 ℃		2.5 GPa, 650 ℃		2.5 GPa, 700 ℃		all *PT*		1 GPa, 600 ℃		2 GPa, 600 ℃		2.5 GPa, 650 ℃		2.5 GPa, 700 ℃	
	Average	σ	Average	σ	Average	σ	Average	σ	Average	σ	Average	σ	Average	σ	Average	σ
SiO_2 [wt%]	< 0.12		< 0.12		< 0.12		41	6	< 0.12		< 0.12		< 0.12		< 0.12	
TiO_2 [wt%]	< 0.03		< 0.03		< 0.03		2.9	0.0	< 0.03		< 0.03		< 0.03		< 0.03	
Al_2O_3 [wt%]	< 0.12		< 0.12		< 0.12		53	8	< 0.12		< 0.12		< 0.12		< 0.12	
Cr_2O_3 [wt%]	< 0.03		< 0.03		< 0.03		6	5	< 0.03		< 0.03		< 0.03		< 0.03	
FeO [wt%]	7.7	0.5	7.9	0.6	7.4	0.5	0.7	0.6	9.8	0.7	9	1	8.9	0.4	9.3	0.5
MnO [wt%]	< 0.03		0.1	0.1	< 0.03		< 0.03		< 0.03		< 0.03		0.1	0.1	< 0.03	
MgO [wt%]	40.9	0.4	41.0	0.7	40.9	0.6	1.2	0.9	39	1	39	1	39.9	0.5	39.8	0.6
CaO [wt%]	1.1	0.6	0.8	0.5	1.4	0.6	0.2	0.1	1	1	2	2	1.1	0.6	1.0	0.9
NiO [wt%]	< 0.04		< 0.04		< 0.04		< 0.04		< 0.04		< 0.04		< 0.04		< 0.04	
Na_2O [wt%]	< 0.02		< 0.02		< 0.02		2.1	0.3	< 0.02		< 0.02		< 0.02		< 0.02	
K_2O [wt%]	< 0.02		< 0.02		< 0.02		4.1	0.3	< 0.02		< 0.02		< 0.02		< 0.02	
P_2O_5 [wt%]	< 0.03		< 0.03		< 0.03		1.0	0.3	< 0.03		< 0.03		< 0.03		< 0.03	
Total [wt%]	49.73	0.08	49.8	0.2	49.7	0.1	100		50.2	0.2	50.2	0.2	50.0	0.1	50.1	0.1
Mg#	90.5	0.5	90.2	0.7	90.8	0.7			87.7	1.0	88	1	88.9	0.5	88.4	0.6

	Chlorite zone 2+3		Talc zone 2+3		Talc zone 2+3		Talc zone 2+3		Talc zone 2+3		Talc zone 2+3		Talc zone 2+3		Talc zone 2+3	
	All *PT*		1 GPa, 600 ℃		2 GPa, 600 ℃		2 GPa, 650 ℃		2.5 GPa, 650 ℃		2.5 GPa, 650 ℃		2.5 GPa, 700 ℃		2.5 GPa, 700 ℃	
			Replacing olivine		Replacing opx		Replacing olivine		Replacing olivine		Replacing opx		Replacing olivine		Replacing cpx	
	Average	σ	Average	σ	Average	σ	Average	σ	Average	σ	Average	σ	Average	σ	Average	σ
SiO_2 [wt%]	34	1	62.2	0.1	59.5	1.0	61	3	61	2	58.4	0.9	61	4	55.1	0.4
TiO_2 [wt%]	< 0.03		< 0.03		< 0.03		< 0.03		< 0.03		< 0.03		< 0.03		< 0.03	
Al_2O_3 [wt%]	16	1	< 0.12		4.3	0.9	< 0.12		0.3	0.4	3.2	0.5	0.4	0.5	0.4	0.4
Cr_2O_3 [wt%]	1	1	< 0.03		0.1	0.2	< 0.03		< 0.03		< 0.03		< 0.03		< 0.03	
FeO [wt%]	4.0	0.4	3.3	0.4	4.1	0.4	2	2	3.9	0.7	3.8	0.2	4	2	6.7	0.8
MnO [wt%]	< 0.03		< 0.03		< 0.03		< 0.03		< 0.03		< 0.03		< 0.03		< 0.03	
MgO [wt%]	33	2	29.8	0.5	27.2	0.9	33	5	30	1	30	1	30	2	33.1	0.9
CaO [wt%]	< 0.03		< 0.03		0.1	0.5	< 0.03		< 0.03		< 0.03		< 0.03		< 0.03	
NiO [wt%]	< 0.04		< 0.04		< 0.04		< 0.04		< 0.04		< 0.04		< 0.04		< 0.04	
Na_2O [wt%]	< 0.02		< 0.02		< 0.02		< 0.02		< 0.02		< 0.02		< 0.02		< 0.02	
K_2O [wt%]	< 0.02		< 0.02		< 0.02		< 0.02		< 0.02		< 0.02		< 0.02		< 0.02	
P_2O_5 [wt%]	< 0.03		< 0.03		< 0.03		< 0.03		< 0.03		< 0.03		< 0.03		< 0.03	
Total [wt%]	87.3	0.1	95.32	0.01	95.34	0.02	95.2	0.1	95.32	0.02	95.30	0.02	95.31	0.03	95.27	0.02
Mg#	93.6	0.9	94.1	0.8	92.2	0.7	97	4	93.1	1.0	93.3	0.4	93.2	2.4	90	1

	Talc zone 2+3		Antigorite zone 3		Antigorite zone 3	
	2.5 GPa, 700 ℃		2 GPa, 600 ℃		2.5 GPa, 650 ℃	
	replacing opx					
	Average	σ	Average	σ	Average	σ
SiO_2 [wt%]	60	1	41	3	43	2
TiO_2 [wt%]	< 0.03		< 0.03		< 0.03	
Al_2O_3 [wt%]	2.5	0.2	< 0.12		0.2	0.2

Table 3 (continued)

	Talc zone 2 + 3		Antigorite zone 3		Antigorite zone 3	
	2.5 GPa, 700 ℃		2 GPa, 600 ℃		2.5 GPa, 650 ℃	
	replacing opx					
	Average	σ	Average	σ	Average	σ
Cr_2O_3 [wt%]	0.4	0.5	< 0.03		< 0.03	
FeO [wt%]	3.4	0.1	6.7	0.8	7.1	0.5
MnO [wt%]	< 0.03		< 0.03		< 0.03	
MgO [wt%]	29	1	39	2	36	2
CaO [wt%]	< 0.03		0.1	0.3	0.7	1.0
NiO [wt%]	< 0.04		< 0.04		< 0.04	
Na_2O [wt%]	< 0.02		< 0.02		< 0.02	
K_2O [wt%]	< 0.02		< 0.02		< 0.02	
P_2O_5 [wt%]	< 0.03		< 0.03		< 0.03	
Total [wt%]	95.32	0.03	87.3	0.1	87.5	0.1
Mg#	93.84	0.05	91.3	0.7	90.2	0.6

The Mg# of magnesite formed together with quartz and kyanite in zone 1 is with ~ 90.5 for all *PT* higher compared to magnesite formed with chlorite and talc in zone 2 and 3 (Mg# ~ 88). The Al_2O_3 and Cr_2O_3 content in talc reflects the replaced primary silicate as it is higher when talc replaces pyroxenes compared to talc replacing Al- and Cr-poor olivine

*Per EDS

the attempt to re-equilibrate. Secondary orthopyroxene and clinopyroxene form rims around primary orthopyroxene and clinopyroxene crystals, respectively. Secondary orthopyroxene has lower Al (variation (Δ) of $Al_2O_3 = 1.5$ wt%; run 36), lower Ca ($\Delta CaO = 0.6$ wt%) and lower Mg# ($\Delta Mg\# = 6.3$) than the primary orthopyroxene. Secondary clinopyroxene in run 36 is depleted in Al ($\Delta Al_2O_3 = 2.4$ wt%), Na ($\Delta Na_2O = 0.4$ wt%) and Mg# ($\Delta Mg\# = 1.5$) and enriched in Ca compared to the primary clinopyroxene composition.

Spinel

Primary spinel ($Mg_{0.79}Fe_{0.25}Cr_{0.38}Al_{1.58}O_4$), in the quartz-layer (run 37) and remaining spinels in the experiments, if present, have similar composition (variation ± 0.01 a.p.f.u. for 4 oxygen).

Distribution of trace elements

Carbonates

Carbonates are the main hosts for Sr and Ba among the secondary phases (Sieber et al. 2018). Their concentrations monitor the evolution of the fluid and reaction progress, because they are mainly contributed by the fluid (see "Experimental setup"; Sieber et al. (2020)). Magnesite grains in zone 1 are enriched in Sr and Ba compared to magnesite in zones 2 and 3. Sr and Ba in magnesite of zone 2 are zoned (Fig. 6d). The highest concentrations are found at the contact with talc and decrease continuously towards zone 1. At the contact with talc, the concentrations of Sr and Ba in magnesite approach the concentrations observed for magnesite in zone 1 (Fig. 6d). Across the magnesite + antigorite bearing zone 3 (Fig. 6c), Sr and Ba decrease within the first ~ 120 µm and remain afterwards almost constant.

Talc

Zone 2: The trace element content in talc in zone 2 is characteristic for the replaced primary phase. For instance, clinopyroxene crystals contain the highest Cr concentrations among primary silicates, and talc associated with the replacement of clinopyroxene is enriched in Cr (5684 ± 331 ppm) compared to talc replacing enstatite (1884 ± 1165 ppm) and olivine (116 ± 42 ppm). Compared to pyroxenes, olivine grains contain more Ni and Co and talc associated with the replacement of olivine is enriched in Ni (3316 ± 1152 ppm) and Co (152 ± 54 ppm) compared to talc replacing clinopyroxene (Ni = 273 ± 28 ppm; Co = 16 ± 1 ppm) and orthopyroxene (Ni = 409 ± 242 ppm; Co = 32 ± 16 ppm). Based on their Mn content, talc grains replacing olivine (972 ± 413 ppm) and orthopyroxene (682 ± 229 ppm) cannot be distinguished, but talc replacing clinopyroxene shows lower Mn concentrations (473 ± 14 ppm). Values reported in this paragraph reflect the average trace element concentration in talc measured in run 34, but are representative for all experiments.

Change in volatile fluid composition

The observed formation of carbonates and hydrous phases provide evidence that fluid composition changes during the experiments. Next to carbonation, minor CO_2 might be consumed by the formation of elemental carbon (graphite with poor crystal symmetry) and methane (CH_4) (Sieber et al. 2020). A free fluid phase and elemental carbon were observed in all experiments. Elemental carbon is present in reaction zone 1 and 2 but absent in zone 3 (Fig. 5).

Here we compare the calculated fluid composition to the measured post run fluid as analysed by gas-chromatography of run 42 for which the 3D phase proportions were also determined by X-ray computed tomography. For the calculations, we first followed the approach applied by Sieber et al. (2020), calculating the CO_2–H_2O fluid composition responsible for mineral carbonation (Table 2). This calculation assumes that all H_2 is consumed in the formation of elemental carbon at the onset of the experiment and neglects minor amounts of methane. Accordingly, the carbon-saturated fluid in run 42 contains 83 mol% H_2O and 17 mol% CO_{2aq}. In a second step, this CO_2–H_2O composition was used to calculate the modal proportions and fluid composition under the experimental *PT* conditions using perple_X. We allowed for redox processes by treating the fluid as a graphite-saturated, multi-species COH-fluid. The calculated fluid composition contains 99.4 mol% H_2O, 0.6 mol% CO_{2aq} and 0.001 mol% CH_4. The post-run fluid of run 42, as analysed by gas-chromatography, contains 96.6 mol% H_2O, 1.4 mol% CH_4 and 2 mol% CO_{2aq}. The somewhat higher amount of CO_{2aq} in the measured fluid compared to the calculated fluid composition may imply that carbonation is not completed after 55 h at 2 GPa and 600 °C. According to the modelling, the solids of run 42 should contain 40 vol% antigorite, 28 vol% carbonates, 26 vol% orthopyroxene, 4 vol% clinopyroxene and 2 vol% olivine. Segmentation of the CT scan resulted in 34 vol% orthopyroxene, 20 vol% olivine and secondary orthopyroxene, 17 vol% antigorite (and some magnesite), 15 vol% talc, 12 vol% magnesite and 2 vol% kyanite. The algorithms used in the phase segmentation of the CT-raw data may overlook small roundish grains with poor phase contrast to the surrounding phases. Thus, particularly magnesite grains intermingled with talc and antigorite in reaction zones 2 and 3, respectively, are underestimated. The mismatch between the calculations and the observations from the experiment is likely related to the maintenance of several reaction zones in the experiments, whereas the calculation assumes overall equilibrium.

Change in density, volume and porosity

Reaction zones are fluid permeable allowing the replacement of primary silicates to continue over time. Pore spaces are visible in BSE-images of all reaction zones and pronounced in zone 1 (Fig. 1). The high porosity in zone 1 is related to the lack of quartz. Pore space accounts for 11 vol% of the recovered core of run 42 as obtained by segmentation of the CT-scan. The density of secondary phases is lower than that of primary phases. As density is defined by the quotient of mass and volume, a reduction of the bulk density means that peridotite alteration can either be written as isochemical replacement, whereby the volume has to increase, or as volume conservative reactions if some mass is transported by the fluid elsewhere (Kelemen et al. 2011; Majumdar et al. 2016; Putnis 2009). The changes of the core's volumes were constrained by measuring the dimensions of the cores before and after the experiment and, in a more indirect approach, using density maps computed with XMapTools (details are summarized in the supplementary information). The volume increased by ~ 7–10% in experiments performed with a fluid/rock-ratio < 0.5 and relatively small amounts of CO_{2aq} (e.g., run 36 and 42).

In contrast, in experiments starting with fluid/rock-ratios > 0.54 and the highest CO_{2aq} (run 37 and 39), the volume of the rock-core was conserved and significant amounts of SiO_{2aq} were transported by the fluid and precipitated at the bottom of the capsules (quartz-layers). The core's bulk densities before and after those experiments were calculated using density maps computed with XMapTools (see supplementary information). Accordingly, the core's bulk densities decreased by ~ 12%. Assuming a volume conservative replacement, the mass needs to be reduced by ~ 12 wt%. The quartz layer has a height of ~ 0.5 mm resulting in a volume of ~ 6 mm^3 (if the entire bottom of the capsule is covered with quartz) or a mass of ~ 15 mg. This mass equals ~ 13 wt% of the mass of the peridotite core. The results correlate well and demonstrate that the replacement conserved the overall volume of the core by reducing its mass (mainly silica).

Permeability within all reaction zones must be sufficient to allow the reaction to proceed over time, demonstrating that interconnected porosity was created. In addition, fractures pre-existing in the peridotite core and formed during the experiment facilitate the reaction. We propose that they might be distinguishable based on the mineral assemblage along such fluid pathways. Pre-existing fractures can contain all reaction zones, while fractures that opened during the cause of the experiment do not develop a zone 1 (magnesite + quartz) alteration. Decompression can also introduce fractures, which lack any kind of secondary assemblage.

Discussion

Efficient peridotite alteration

The observed extents of peridotite alteration are remarkable, particularly when they are compared to those reported from hydrothermal experimental studies up to ~ 200 °C conducted in the context of in situ mineral carbonation. For instance, using peridotite cores in hydrothermal batch experiments up to 200 °C and between 130 and 180 bar, carbonate bearing reaction zones are on the order of tens of µm in width after 15–25 days (Hövelmann et al. 2012). Given such marginal replacement, the formation of reaction zones of ~ 0.05–1.1 mm in width within 8 days, is noteworthy. According to phase segmentation of the CT-scan, nearly 50% of primary silicates are already replaced within 55 h at 650 °C, 2.5 GPa, an initial CO_{2aq} of 17 mol% and fluid/rock-ratio of 0.54 (run 42). Moreover, the CO_{2aq} has been reduced from 17 to 2 mol%. Considering that the calculated equilibrium value for this experiment is at 0.6 mol%, the reaction progress is above 90%. The extent of peridotite alteration approaches the replacement of serpentinites for similar *PTt*-conditions, fluid-composition and fluid/rock-ratios (Sieber et al. 2020). Several parameters such as temperature, fluid composition and fluid/rock-ratio may affect the efficiency of peridotite alteration, but the set of performed experiments does not allow discussion of the individual effects of these parameters on the reaction efficiency. However, we do observe that fluid driven alteration of peridotites within greenschist, blueschist to low-grade eclogite facies conditions and for the investigated fluid composition and fluid/rock-reactions is significant in sequestrating volatiles even under the full complexity of the natural peridotite (natural grain sizes, grain shapes, porosity).

For alteration of peridotites to be efficient, the infiltrating fluid must be able to reach fresh and unreacted surface of primary phases (Putnis 2009). Therefore, interconnected porosity must be present within reaction zones and/or cracking of primary phases must expose unaltered surface area to the fluid. In our experiments we observe both: the formation of fluid permeable reaction zones and the opening of fractures depending, for instance, on the fluid/rock-ratio and $X_{CO_2}^{fluid}$.

Opening of fluid pathways

For an isochemical alteration of peridotites, a large volume increase is expected building up stress that, if sufficient, can fracture the rock (Kelemen and Matter (2008). Alternatively, the volume of peridotites might be conserved if mass (mainly SiO_{2aq} in our experiments) is transported away (Kelemen and Hirth 2012). We propose that new fluid pathways opened during the experiments and that alteration increased the volume of solids by ~ 10% for experiments performed with a fluid/rock-ratio ≤ 0.54 and relatively small, initial amounts of CO_{2aq} (e.g., run 36, 42). We observed reaction zones which cut through a grain of a primary silicate and contain zone 2 and 3 but lack elemental carbon and zone 1. These reaction pathways are assumed to form when primary phases crack during the experiment exposing new reaction pathways. The lack of elemental carbon and zone 1 implies that those cracks did not exist before the experiment, but developed and opened during the experiment (Figs. 1, 2). We determined the maximal volume increase in the full carbonation of the peridotite (sample PO6) using perple_X to calculate the bulk densities of the solids in zone 1 and 2. Using those densities and assuming zero porosity within reaction zones, we calculated the volume change during carbonation of olivine, orthopyroxene and clinopyroxene to zone 1 and 2 at 600 °C, 2 GPa and $X_{CO_2}^{fluid}$ of 0.1 and 0.03, respectively (Table S1 in the supplementary information). Using the abundance of primary silicates of the peridotite (PO6), we calculated a volume increase of 50 vol% and 31 vol% for the full carbonation of PO6 to zone 1 and 2, respectively. This observed volume increase is smaller, because some primary phases remained and because the reaction (particularly the formation of zone 1) did not occur isochemically, as assumed in the calculation. The enhanced solubility of quartz into a COH-fluid that is becoming more aqueous as carbonation proceeds may hamper stress build-up to levels sufficient to fracture the rock. This may explain, why fluid pathways opened during the experiment lack quartz and kyanite. The opening of additional fluid pathways enables the COH-fluid to reach and react with fresh surface of primary silicates facilitating the reaction progress. In natural settings, fractures are found in completely carbonated peridotites (soapstones and listvenites), but are more aided by tectonic uplift rather than reaction driven cracking (Falk and Kelemen 2015; Kelemen and Hirth 2012; Kelemen and Matter 2008). Cracks might further be associated with thermal expansion during heating (Fredrich and Wong 1986). For hydration of peridotites, the opening of fluid pathways was associated with tectonic stress (e.g., Andréani et al. (2007)) but can also generate stress sufficient for fracturing of the rock (Iyer et al. 2008; Plümper et al. 2012b).

Fluid permeable reaction zones

There is good evidence for fluid permeable reaction zones. First, pore space is visible in BSE-images and in the CT-scan. Second, the composition and texture of secondary phases and reaction zone, respectively, imply that the

reaction zones are fluid permeable. In addition, the precipitation of quartz at the bottom of the capsules (away from the peridotite core) demonstrates enormous transport of SiO_{2aq}. Near maintenance of the initial volume of the peridotite core in experiments started under fluid/rock-ratios > 0.54 and with the highest CO_{2aq} concentrations accompanies such large-scale SiO_{2aq} transport. The transport of Mg^{2+}_{aq}, Fe^{2+}_{aq} and SiO_{2aq} across zone 2 is evident by the gradual zonation of the Mg# of talc and magnesite (Fig. 4c, d). As reaction zone 2 evolves, Mg^{2+}_{aq} and Fe^{2+}_{aq} are transported over increasingly longer distances away from the reactive surface and through existing talc and magnesite (see "Replacement mechanism"). For this process to continue, zone 2 must be fluid permeable.

Replacement mechanism

When primary silicates are in direct contact with the COH-fluid, they partially dissolve and the fluid may become locally (super-) saturated with respect to the more stable, secondary phase(s) resulting in their precipitation at the reaction interface. Pseudomorphic replacement (e.g., Fig. 1) supports such an interface coupled dissolution–reprecipitation process (Putnis 2009; Putnis and John 2010; Putnis and Putnis 2007) at least for zone 2 and 3. It has been concluded that the main re-equilibration mechanism in fluid present metamorphic replacement is dissolution–reprecipitation (Putnis (2009), Putnis and Austrheim (2010) and references therein).

The survival of distinct reaction zones clearly demonstrates that a system-wide equilibrium has not been obtained. Instead, the different reaction zones are out of equilibrium with each other. However, during their formation local equilibrium between the primary silicate and the product assemblage might be assumed, but requires sufficient exchange between them (Plümper et al. 2012a). With respect to Ca, Mg, Fe and Al, primary olivine and orthopyroxene may dissolve congruently maintaining the volatile-free, major element compositions. For instance, the Ca content in magnesite can be used to identify the replaced primary silicate as Ca released from the primary silicate is not distributed in the overall fluid but incorporated (locally) into newly formed magnesite. Furthermore, the Al, Cr and Ni contents in talc are indicative for the replaced silicate and affected by *PT*-conditions. In zone 2, magnesite and talc occur locally separated from each other (Figs. 4a, b, 5a). Assuming congruent dissolution, this spatial separation may imply earlier talc saturation than magnesite saturation within the interfacial fluid volume. As the reaction proceeds, the reactive interface moves towards the centre of the primary silicates and Mg^{2+}_{aq} and Fe^{2+}_{aq} must be transported over increasing distances (growing talc) to form magnesite in zone 2. Although magnesite and talc crystallize apart from each other, the systematic, gradual change of Mg# may suggest local equilibrium. For instance, the Mg# of magnesite increases from ~ 88 to ~ 89 and Mg# of talc decreases from the contact with magnesite towards the centre of partially replaced grains (Fig. 4). This zonation implies opposite growth directions of magnesite and talc. The contact between magnesite and talc in zone 2 is interpreted to mark the beginning of the replacement of primary silicates to zone 2 and thus represents the former grain boundary at the onset of the formation of zone 2. From here, magnesite grew outwards (to the left) and talc grew inwards (to the right in Figs. 4, 6). In contrast to Mg and Fe, which are liberated by the dissolution of primary phases, the fluid provides Sr^{2+}_{aq}, Ba^{2+}_{aq} (and Ca^{2+}_{aq} in the replacement of olivine). Thus, the distribution of those elements can be used to monitor the reaction progress over time (Sieber et al. 2020). Ca, Sr and Ba are enriched in early formed magnesite and highest in magnesite associated with zone 1. The zonation of these elements in magnesite in zone 2 with the highest concentrations adjacent to talc supports the opposite growth direction of magnesite and talc in zone 2 and further supports sufficient fluid transport across the reaction zone. Enhanced diffusional element exchange of major and minor elements was also reported for carbonation of hydrated peridotites from the Oman ophiolithe (Beinlich et al. 2020).

The low olivine/orthopyroxene-ratios observed in our post-run assemblies demonstrate efficient replacement of olivine compared to orthopyroxene particularly, since olivine is the most abundant phase in the natural harzburgite. Enhanced and faster carbonation of olivine compared to pyroxene is known from experimental studies conducted in the context of mineral carbonation (under much lower pressures < 200 bar) (Hövelmann et al. 2012; Kelemen et al. 2011; Lacinska et al. 2017). Furthermore, investigating the simultaneous carbonation and hydration of olivine grains in a closed system, Lafay et al. (2014) showed that carbonation is faster but that hydration occurs over longer times. This is further supported by recent results indicating that hydration of olivine becomes faster in the presence of pyroxene (Aarrestad et al. 2021).

Evolution of reaction zones

As outlined above ("Replacement mechanism"), carbonation occurs at the reactive interface, where primary silicates are in direct contact with the fluid. Thus, the spatial distribution of reaction zones and relicts of primary phases are controlled by the migration of the COH-fluid along grain boundaries into the peridotite-core. Replacement of primary silicates starts at their grain boundaries and proceeds towards the

centre of the grains. The formed reaction zones and mineral modes within the reaction zones depend on the composition of the fluid (e.g., CO_{2aq}, SiO_{2aq}; see next section "Carbonation reactions and fluid composition") at the reaction interface (Putnis 2009; Putnis and John 2010; Putnis and Putnis 2007). The spatial variation from magnesite + quartz at the rim (zone 1) to magnesite + talc + chlorite (zone 2) and either serpentine + magnesite or talc ± chlorite ± magnesite (zone 3) towards the centre of the primary silicate could represent a temporal evolution (rim first, centre later) or a chemical gradient across the reaction zone. The latter hypothesis would mean that the composition of the fluid at the reactive interface varies relative to the overall fluid composition. In contrast, a temporal evolution demands sufficient fluid exchange through the reaction zones and benefits from fluid permeable reaction zones.

Next to reaction zones being sufficiently fluid permeable allowing mass and fluid exchange across reaction zones, a temporal evolution is further supported by the trace element distribution into magnesite. Magnesite is the main host of Ca, Sr and Ba which are mainly contributed by the fluid (the concentration of Sr and Ba in primary silicates is neglectable compared to their concentration in the fluid; Table 1). Consequently, early formed magnesite is enriched in those elements compared to magnesite formed from a more evolved fluid having lower Ca^{2+}_{aq}.Sr^{2+}_{aq} and Ba^{2+}_{aq} concentrations. For the given *PT*, the partitioning of these elements between magnesite and COH-fluid is (within the uncertainty) not affected by a change in CO_{2aq} and SiO_{2aq} (Sieber et al. 2018). Thus, the decreasing trace element content of magnesite from zone 1, to zone 2 and zone 3 reflects a temporal evolution of the reaction zones with a fluid that becomes depleted in trace elements (and CO_{2aq}) as carbonation proceeds. Earlier time series performed with the same experimental setup on the fluid driven carbonation of serpentinites cores also support a temporal evolution of the reaction zones (Sieber et al. 2020).

Carbonation reactions and fluid composition

The development of reaction zones can be used to track the evolution of the fluid over time and can be modelled assuming local equilibrium between the fluid and the primary silicate. The replacement of primary silicates consumes CO_{2aq} and H_2O in the formation of secondary phases reducing X_O^{fluid}. A C-saturated fluid with $X_O^{fluid}>1/3$ contains mostly CO_{2aq} and H_2O. Thus, by neglecting minor amounts of CH_4 in the experimental fluid, X_O^{fluid} can be converted into a molar $CO_2/(CO_2+H_2O)$ ratio ($X_{CO_2}^{fluid}$) (Fig. 7). The evolution of the graphite-saturated COH-fluid can be tracked from the observed mineral assemblages. As already noted in earlier studies (Johannes 1969; Kerrick 1974), under high $X_{CO_2}^{fluid}$ divalent cations (e.g., Ca, Mg, Fe) are primarily incorporated into carbonate minerals and thus the Si-content in secondary silicates increases with increasing $X_{CO_2}^{fluid}$ (Fig. 7). Consequently, under the initially highest $X_{CO_2}^{fluid}$ = 0.17–0.26 (X_O^{fluid} = 0.41–0.46), zone 1 formed under Si-saturation (quartz formation). As CO_{2aq} is consumed in the formation of carbonates, the fluid becomes more aqueous (decreasing $X_{CO_2}^{fluid}$, X_O^{fluid}) leading to the formation of talc + magnesite ± chlorite (zone 2, orange shaded area in Fig. 7). X_O^{fluid} and $X_{CO_2}^{fluid}$ decrease further as H_2O and CO_{2aq} are consumed when talc and magnesite, respectively, are formed. Compared to zone 2, zone 3 (blue shaded area in Fig. 7) is stable under lower X_O^{fluid} and further reduced quartz activity. The measured fluid of run 42 (2.5 GPa, 650 °C) contains 2 mol% CO_{2aq} (X_O^{fluid} = 0.336), which is in agreement with the calculations considering that the reaction completed with the formation of zone 3 after nearly 50 vol% of primary silicates were replaced within 55 h (phase proportions are according to segmentation of the CT-scan).

The experimental results show that the COH-fluid driven carbonation and hydration of spinel-bearing harzburgite at 1–2.5 GPa and 600–700 °C is effective at sequestering H_2O and CO_{2aq}. The abundance of magnesite and the secondary assemblage depend on the molar proportion of CO_{2aq} ($X_{CO_2}^{fluid}$) (Fig. 7). The modelling and the observations from the experiments show that the amount of carbonates increases over time until $X_{CO_2}^{fluid}$ in the fluid falls below the required $X_{CO_2}^{fluid}$ to cause carbonation. Hydration and silicification commence subsequent to carbonation (Fig. 7), evidenced in carbonate poor to carbonate free assemblages (zone 3; blue shaded area in Fig. 7).

It should be noted that the precipitation of elemental carbon in our experiments not only reduces CO_{2aq} but also may affect the solubility of primary silicates and the amount of SiO_{2aq} (Tiraboschi et al. 2017; Tumiati et al. 2017). The amount of dissolved Si in graphite-saturated COH-fluids in equilibrium with quartz and graphite (Tumiati et al. 2017) is much higher than in graphite-free COH-fluids (Newton and Manning 2000). The solubility of quartz into CO_2–H_2O-fluid increases with increasing H_2O content (Newton and Manning 2000). The dissolution of quartz into a fluid that is becoming more aqueous as carbonation proceeds, was reported from carbonation of serpentine in graphite-free CO_2–H_2O-fluids (Sieber et al. 2018) and C-saturated CO_2–H_2O–CH_4-fluids (Sieber et al. 2020). By analogy with our earlier studies, we assume that quartz formed in zone 1 partially dissolves as carbonation proceeds. Some dissolved SiO_{2aq} contribute to the conversion of olivine into serpentine and orthopyroxene into talc.

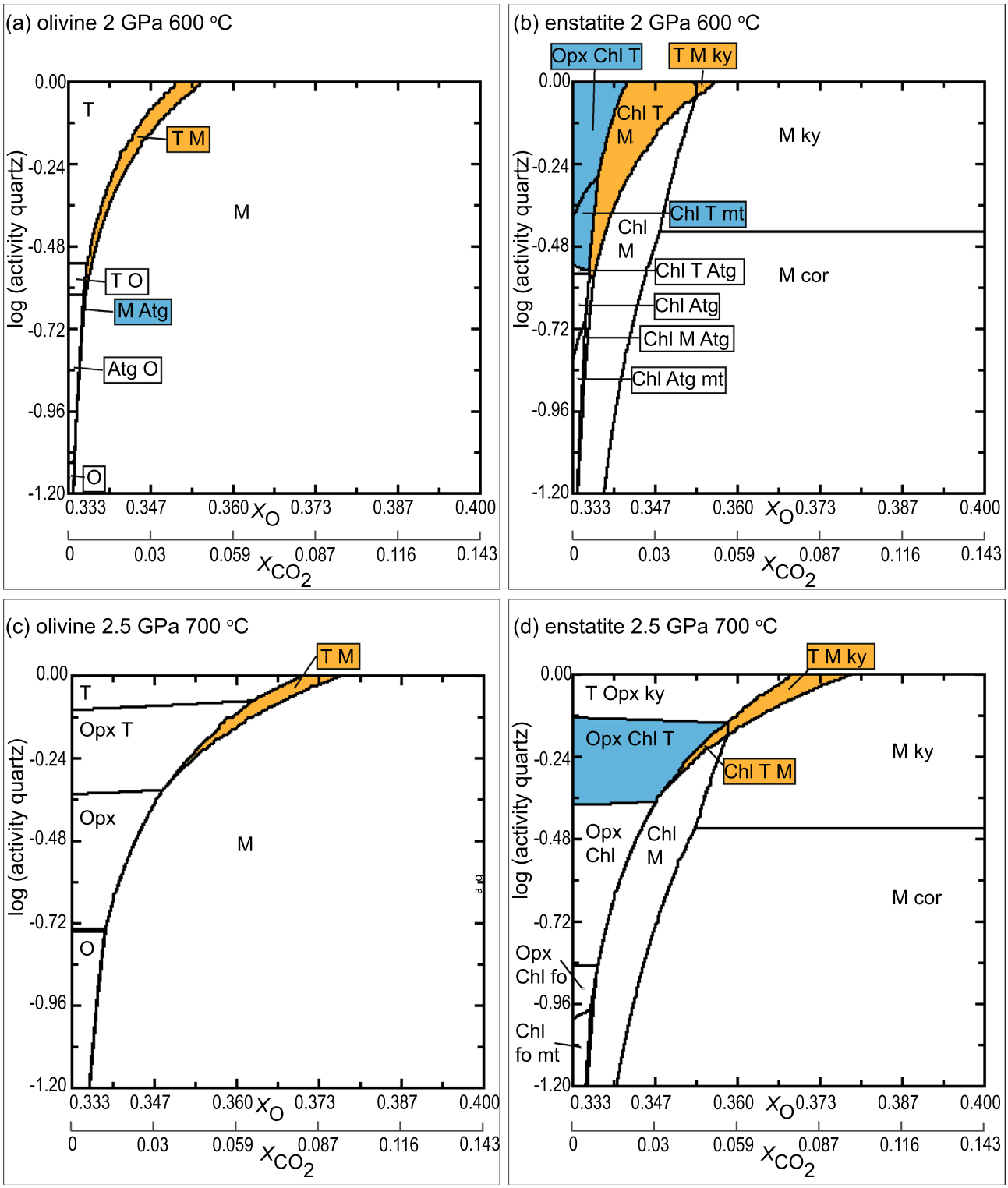

Fig. 7 Activity of quartz versus X_O^{fluid} phase diagrams at 2 GPa and 600 °C (within antigorite stability) and 2.5 GPa and 700 °C (above antigorite stability) for **a**, **c** olivine with 50.1 wt% MgO and 9 wt% FeO and **b**, **d** for orthopyroxene with 33.3 wt% MgO, 5.8 wt% FeO and 4.3 wt% Al_2O_3. Observed phase assemblages of reaction zone 2 are highlighted in orange and of zone 3 in blue. The sequence of reaction zones (from 1 to 2 and 3) can be explained by decreasing X_O^{fluid} and quartz activity over time. *Ant* Antigorite, *Chl* chlinochore, *ky* kyanite, *Mag* Magnesite, *mt* magnetite, *Ol* Olivine, *Opx* Orthopyroxene. Capital letters refer to solid solutions; small letters are used for endmember compositions

Conclusions and implications

This experimental study demonstrates that metasomatism of the dry forearc mantle is a self-promoting process that may, over time, cause large scale alteration of peridotites within and above a subducting slab. COH-fluid released during devolatilization of subducting lithologies (particularly sediments and altered oceanic crust), will, metasomatise surrounding peridotites efficiently. In a previous study we have shown that the carbonation of a serpentinised mantle wedge is very efficient as the carbonation reaction is concomitant with serpentine dehydration and induces a small negative volume change that promotes reaction progress (Sieber et al. 2020). As both the hydration and carbonation of peridotites result in a large volume increase (at constant mass of non-volatile elements), we expected an inefficient fluid–rock reaction of slab volatiles with a peridotite mantle wedge. Instead, we observe that hydration and carbonation of peridotites is also fast. In run 42 at 650 °C, 2 GPa, 90% of the CO_{2aq} of the initial fluid has been sequestered within the 55 h of the experiment and nearly 50% of the initial phases have been replaced by secondary carbonates and hydrous phases. Reaction zones are fluid permeable, because mass (e.g., SiO_{2aq}) is transported by the fluid and fresh reactive surfaces of primary silicates are exposed as the volume increase builds up sufficient stress for reaction driven cracking. Both mechanisms promote peridotite alteration and have been observed in our experiments.

Considering an open system and steady COH-fluid flux along veins, peridotite replacement will occur within the vein and where the COH-fluid migrates pervasively into the peridotite. With increasing penetration depth of the fluid into the rock and forward propagation of the vein, $X_{CO_2}^{fluid}$ will decrease leading to the formation of metasomatic reaction fronts (sub-) parallel to the vein. The contact between peridotite and secondary assemblage will be sharp as observed in the experiments. Under a steady fluid flux in an open system, a chemical gradient from the vein across the metasomatic reaction zones will develop. This is different to the experiments (closed system), where the composition of the overall fluid changed as carbonation proceeded over time. In natural systems, the aspect ratios of reaction zones will depend on the rate of COH-fluid influx, $X_{CO_2}^{fluid}$ and all reaction zones may evolve over time. In experiments with highest fluid/rock-ratios, as can be assumed for channelized fluid flow, enormous amounts of dissolved silica are transported. Such transport may also occur in open systems causing silicification (and hydration) elsewhere (further away from the injection of the COH-fluid into the peridotite).

Furthermore, metasomatism of peridotites is efficient in sequestering volatiles into newly formed elemental carbon, carbonates, talc, antigorite and chlorite as the extent of replacement is remarkable. Therefore, carbonation of mantle wedge peridotites has to be considered in the assessment of the return flux from the subducted slab to the surface (c.f. Kelemen and Manning (2015)). Moreover, carbonation of peridotites sequesters, to some extent, fluid mobile elements such as Sr_{aq}^{2+} and Ba_{aq}^{2+} from reactive COH-fluids into newly formed carbonates (Sieber et al. 2018). The chemical (and isotopic) signature of a carbonated mantle wedge may thus be imposed by metasomatizing fluids liberated from the subducting oceanic crust.

Supplementary Information The online version contains supplementary material available at https://doi.org/10.1007/s00410-022-01905-w.

Acknowledgements We are grateful to L. Beeching, F. Brink, D. Clark, P. Lanari, C. Le Losq, J. Middleton, R. Rapp, D. Scott, E. Seccombe, P. Tollan and M. Turner for their assistance in analytical and experimental work. This study was funded by an ARC Discovery Grant (DP14010089) to G. M. Yaxley and J. Hermann, and by an ANU PhD stipend and the Mervyn and Katalin Paterson fellowship to M. J. Sieber. Furthermore, we like to thank C. Tiraboschi and one anonymous reviewer for constructive comments and T. John for editorial handling of the paper.

Funding Open Access funding enabled and organized by Projekt DEAL.

References

Aarrestad I, Plümper O, Roerdink D, Beinlich A (2021) Feedback mechanisms in mineral replacement networks: an experimental investigation of the ultramafic model system. In, vol., pp EGU21–8633

Ague JJ, Nicolescu S (2014) Carbon dioxide released from subduction zones by fluid-mediated reactions. Nat Geosci 7(5):355–360

Andréani M, Mével C, Boullier AM, Escartin J (2007) Dynamic control on serpentine crystallization in veins: constraints on hydration processes in oceanic peridotites. Geochem Geophys Geosyst. https://doi.org/10.1029/2006GC001373

Bebout GE (2013) Metasomatism in subduction zones of subducted oceanic slabs, mantle wedges, and the slab-mantle interface. Metasomatism and the chemical transformation of rock: the role of fluids in terrestrial and extraterrestrial processes. Springer, Berlin, pp 289–349

Bebout G, Barton MD (1989) Fluid flow and metasomatism in a subduction zone hydrothermal system. Geology 17:976–980

Beinlich A, Plümper O, Hövelmann J, Austrheim H, Jamtveit B (2012) Massive serpentinite carbonation at Linnajavri. N-Norway Terra Nova 24(6):446–455

Beinlich A, Plümper O, Boter E, Müller IA, Kourim F, Ziegler M, Harigane Y, Lafay R, Kelemen PB, Team tODPS (2020) Ultramafic rock carbonation: constraints from listvenite core BT1B, Oman Drilling Project. J Geophys Res Solid Earth. https://doi.org/10.1029/2019JB019060

Bjerga A, Konopásek J, Pedersen RB (2015) Talc–carbonate alteration of ultramafic rocks within the Leka Ophiolite Complex, Central Norway. Lithos 227:21–36

Breeding CM, Ague JJ, Bröcker M (2004) Fluid–metasedimentary rock interactions in subduction-zone mélange: Implications for the chemical composition of arc magmas. Geology 32(12):1041–1044

Brovarone AV, Martinez I, Elmaleh A, Compagnoni R, Chaduteau C, Ferraris C, Esteve I (2017) Massive production of abiotic methane during subduction evidenced in metamorphosed ophicarbonates from the Italian Alps. Nat Commun 8:14134

Caciagli NC, Manning CE (2003) The solubility of calcite in water at 6–16kbar and 500–800C. Contrib Miner Petrol 146(3):275–285

Connolly JAD (2005) Computation of phase equilibria by linear programming: A tool for geodynamic modeling and its application to subduction zone decarbonation. Earth Planet Sci Lett 236(1–2):524–541

Connolly J, Cesare B (1993) C−O−H−S fluid composition and oxygen fugacity in graphitic metapelites. J Metamorph Geol 11(3):379–388

Dolejs D, Manning CE (2010) Thermodynamic model for mineral solubility in aqueous fluids: theory, calibration and application to model fluid-flow systems. Geofluids 10(1–2):20–40

Falk ES, Kelemen PB (2015) Geochemistry and petrology of listvenite in the Samail ophiolite, Sultanate of Oman: Complete carbonation of peridotite during ophiolite emplacement. Geochim Cosmochim Acta 160:70–90

Foley SF (2011) A Reappraisal of redox melting in the earth's mantle as a function of tectonic setting and time. J Petrol 52(7–8):1363–1391

Fredrich JT, Wong T-f (1986) Micromechanics of thermally induced cracking in three crustal rocks. J Geophys Res Solid Earth 91(B12):12743–12764

Galvez ME, Beyssac O, Martinez I, Benzerara K, Chaduteau C, Malvoisin B, Malavieille J (2013a) Graphite formation by carbonate reduction during subduction. Nat Geosci 6:473

Galvez ME, Martinez I, Beyssac O, Benzerara K, Agrinier P, Assayag N (2013b) Metasomatism and graphite formation at a lithological interface in Malaspina (Alpine Corsica, France). Contrib Miner Petrol 166(6):1687–1708

Gorman PJ, Kerrick DM, Connolly JAD (2006) Modeling open system metamorphic decarbonation of subducting slabs. Geochem Geophys Geosyst. https://doi.org/10.1029/2005GC001125

Grozeva NG, Klein F, Seewald JS, Sylva SP (2017) Experimental study of carbonate formation in oceanic peridotite. Geochim Cosmochim Acta 199:264–286

Hack AC, Mavrogenes JA (2006) A cold-sealing capsule design for synthesis of fluid inclusions and other hydrothermal experiments in a piston-cylinder apparatus. Am Miner 91(1):203–210

Holland TJB, Powell R (1998) An internally consistent thermodynamic data set for phases of petrological interest. J Metamorph Geol 16(3):309–343

Hövelmann J, Austrheim H, Beinlich A, Anne Munz I (2011) Experimental study of the carbonation of partially serpentinized and weathered peridotites. Geochim Cosmochim Acta 75(22):6760–6779

Hövelmann J, Austrheim H, Jamtveit B (2012) Microstructure and porosity evolution during experimental carbonation of a natural peridotite. Chem Geol 334:254–265

Huizenga J-M (2011) Thermodynamic modelling of a cooling C-O–H fluid–graphite system: implications for hydrothermal graphite precipitation. Miner Deposita 46(1):23–33

Iyer K, Jamtveit B, Mathiesen J, Malthe-Sørenssen A, Feder J (2008) Reaction-assisted hierarchical fracturing during serpentinization. Earth Planet Sci Lett 267(3):503–516

Johannes W (1969) An experimental investigation of the system MgO-SiO ₂ -H ₂ O-CO ₂. Am J Sci 267(9):1083–1104

Kelemen PB, Hirth G (2012) Reaction-driven cracking during retrograde metamorphism: Olivine hydration and carbonation. Earth Planet Sci Lett 345:81–89

Kelemen PB, Manning CE (2015) Reevaluating carbon fluxes in subduction zones, what goes down, mostly comes up. Proc Natl Acad Sci USA 112(30):E3997-4006

Kelemen PB, Matter J (2008) In situ carbonation of peridotite for CO2 storage. Proc Natl Acad Sci USA 105(45):17295–17300

Kelemen PB, Matter J, Streit EE, Rudge JF, Curry WB, Blusztajn J (2011) Rates and mechanisms of mineral carbonation in peridotite: natural processes and recipes for enhanced, in situ CO2 capture and storage. Annu Rev Earth Pl Sc 39(1):545–576

Kerrick DM (1974) Review of metamorphic mixed-volatile (H2O-CO2) equilibria. Am Miner 59(7–8):729–762

Kerrick D, Connolly J (2001a) Metamorphic devolatilization of subducted marine sediments and the transport of volatiles into the Earth's mantle. Nature 411(6835):293

Kerrick DM, Connolly JAD (2001b) Metamorphic devolatilization of subducted oceanic metabasalts: implications for seismicity, arc magmatism and volatile recycling. Earth Planet Sci Lett 189(1):19–29

King HE, Plümper O, Putnis A (2010) Effect of secondary phase formation on the carbonation of olivine. Environ Sci Technol 44(16):6503

Lacinska AM, Styles MT, Bateman K, Hall M, Brown PD (2017) An experimental study of the carbonation of serpentinite and partially serpentinised peridotites. Front Earth Sci 5:73

Lafay R, Montes-Hernandez G, Janots E, Chiriac R, Findling N, Toche F (2014) Simultaneous precipitation of magnesite and lizardite from hydrothermal alteration of olivine under high-carbonate alkalinity. Chem Geol 368:63–75

Lanari P, Vidal O, De Andrade V, Dubacq B, Lewin E, Grosch EG, Schwartz S (2014) XMapTools: a MATLAB©-based program for electron microprobe X-ray image processing and geothermobarometry. Comput Geosci 62:227–240

Majumdar AS, Hövelmann J, Vollmer C, Berndt J, Mondal SK, Putnis A (2016) Formation of Mg-rich olivine pseudomorphs in serpentinized dunite from the mesoarchean nuasahi massif, eastern india: insights into the evolution of fluid composition at the mineral-fluid interface. J Petrol 57(1):3–26

Malvoisin B, Chopin C, Brunet F, Galvez ME (2011) Low-temperature wollastonite formed by carbonate reduction: a marker of serpentinite redox conditions. J Petrol 53(1):159–176

Martin L, Hermann J (2018) Experimental phase relations in altered oceanic crust: implication for C recycling at subduction zones. J Petrol 59(2):299–320

Menzel MD, Garrido CJ, Sanchez-Vizcaino VL, Marchesi C, Hidas K, Escayola MP, Huertas AD (2018) Carbonation of mantle peridotite by CO2-rich fluids: the formation of listvenites in the Advocate ophiolite complex (Newfoundland, Canada). Lithos 323:238–261

Miozzi F, Tumiati S (2020) Aqueous concentration of CO2 in carbon-saturated fluids as a highly sensitive oxybarometer. Geochem Perspect Lett. https://doi.org/10.7185/geochemlet.2040

Molina JF, Poli S (2000) Carbonate stability and fluid composition in subducted oceanic crust: an experimental study on H2O–CO2-bearing basalts. Earth Planet Sci Lett 176(3):295–310

Morgan G, Chou I-M, Pasteris J (1992) Speciation in experimental COH fluids produced by the thermal dissociation of oxalic acid dihydrate. Geochim Cosmochim Acta 56(1):281–294

Newton RC, Manning CE (2000) Quartz solubility in H 2 O-NaCl and H 2 O-CO 2 solutions at deep crust-upper mantle pressures and temperatures: 2–15 kbar and 500–900 C. Geochim Cosmochim Acta 64(17):2993–3005

Padrón-Navarta JA, Sánchez-Vizcaíno VL, Hermann J, Connolly JAD, Garrido CJ, Gómez-Pugnaire MT, Marchesi C (2013) Tschermak's substitution in antigorite and consequences for phase relations and water liberation in high-grade serpentinites. Lithos 178:186–196

Piccoli F, Vitale Brovarone A, Beyssac O, Martinez I, Ague JJ, Chaduteau C (2016) Carbonation by fluid–rock interactions at high-pressure conditions: Implications for carbon cycling in subduction zones. Earth Planet Sci Lett 445:146–159

Piccoli F, Vitale Brovarone A, Ague JJ (2018) Field and petrological study of metasomatism and high-pressure carbonation from lawsonite eclogite-facies terrains, Alpine Corsica. Lithos 304–307:16–37

Plümper O, King HE, Vollmer C, Ramasse Q, Jung H, Austrheim H (2012a) The legacy of crystal-plastic deformation in olivine: high-diffusivity pathways during serpentinization. Contrib Miner Petrol 163(4):701–724

Plümper O, Røyne A, Magrasó A, Jamtveit B (2012b) The interface-scale mechanism of reaction-induced fracturing during serpentinization. Geology 40(12):1103–1106

Poli S (2015) Carbon mobilized at shallow depths in subduction zones by carbonatitic liquids. Nat Geosci 8(8):633–636

Poli S, Franzolin E, Fumagalli P, Crottini A (2009) The transport of carbon and hydrogen in subducted oceanic crust: an experimental study to 5 GPa. Earth Planet Sci Lett 278(3–4):350–360

Putnis A (2009) Mineral replacement reactions. In: Oelkers EH, Schott J (eds) Thermodynamics and kinetics of water-rock interaction, reviews in mineralogy and geochemistry, vol 70. 1. Mineralogical Society of America & Geochemical Society, Chantilly, pp 87–124

Putnis A, Austrheim H (2010) Fluid-induced processes: metasomatism and metamorphism. Geofluids 10(1–2):254–269

Putnis A, John T (2010) Replacement processes in the earth's crust. Elements 6(3):159–164

Putnis A, Putnis CV (2007) The mechanism of reequilibration of solids in the presence of a fluid phase. J Solid State Chem 180(5):1783–1786

Scambelluri M, Bebout GE, Belmonte D, Gilio M, Campomenosi N, Collins N, Crispini L (2016) Carbonation of subduction-zone serpentinite (high-pressure ophicarbonate; Ligurian Western Alps) and implications for the deep carbon cycling. Earth Planet Sci Lett 441:155–166

Sieber MJ, Hermann J, Yaxley GM (2018) An experimental investigation of C-O-H fluid-driven carbonation of serpentinites under forearc conditions. Earth Planet Sci Lett 496:177–188

Sieber MJ, Yaxley G, Hermann J (2020) Investigation of fluid driven carbonation of a hydrated, forearc mantle wedge using serpentinite cores in high pressure experiments. J Petrol. https://doi.org/10.1093/petrology/egaa035

Spandler C, Mavrogenes J, Hermann J (2007) Experimental constraints on element mobility from subducted sediments using high-P synthetic fluid/melt inclusions. Chem Geol 239(3–4):228–249

Stern RJ (2002) Subduction zones. Rev Geophys 40(4):3-1-3–38

Tiraboschi C, Tumiati S, Sverjensky D, Pettke T, Ulmer P, Poli S (2017) Experimental determination of magnesia and silica solubilities in graphite-saturated and redox-buffered high-pressure COH fluids in equilibrium with forsterite + enstatite and magnesite + enstatite. Contrib Miner Petrol 173(1):2

Tumiati S, Tiraboschi C, Sverjensky D, Pettke T, Recchia S, Ulmer P, Miozzi F, Poli S (2017) Silicate dissolution boosts the CO2 concentrations in subduction fluids. Nat Commun 8(1):616

Tumiati S, Tiraboschi C, Miozzi F, Vitale-Brovarone A, Manning CE, Sverjensky DA, Milani S, Poli S (2020) Dissolution susceptibility of glass-like carbon versus crystalline graphite in high-pressure aqueous fluids and implications for the behavior of organic matter in subduction zones. Geochim Cosmochim Acta 273:383–402

Velbel MA, Ranck JM (2008) Etch pits on naturally altered olivine from dunites of the Appalachian Blue Ridge Mountains, North Carolina, USA. Mineral Mag 72(1):145–148